Geochemical Perspectives Letters

Copper isotope fractionation during lower crustal sulfide accumulation

J. Du[1], H. Guo[2*], S. Fang[3], F. Huang[3]

OPEN ACCESS

https://doi.org/10.7185/geochemlet.2545

Abstract

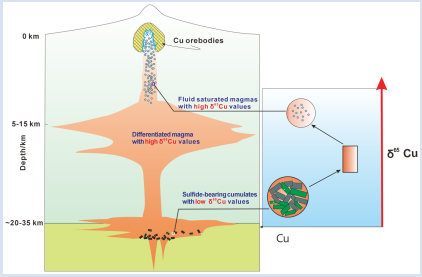

Copper isotopes are key tracers for understanding metal behaviour in porphyry Cu deposits, the dominant global source of the copper. However, although shallow magmatic-hydrothermal processes are well studied, the isotopic fingerprint of sulfide saturation at depth, *i.e.* a pivotal control on porphyry Cu formation, remains enigmatic. We analyse Cu isotopes in sulfide-rich cumulate xenoliths and genetically linked porphyries from Tongling ore district, China. The cumulates are relatively enriched in Cu (263 ± 163 ppm, $n = 4$) and light Cu isotopes (–0.19 ± 0.04 ‰) compared to the porphyries (Cu = 55.4 ± 41.5 ppm, $n = 17$; $\delta^{65}Cu = +0.20 \pm 0.21$ ‰) in porphyries. This dichotomy reflects isotopic fractionation during early sulfide saturation, where sulfides sequester light Cu, enriching residual melts in ^{65}Cu. Synthesising global datasets, we identify a systematic $\delta^{65}Cu$ enrichment trajectory from mantle sources through lower crustal cumulates (–0.19 ‰) to upper crustal porphyries (+0.20 ‰). This depth dependent isotopic stratification implies that near surface ^{65}Cu enrichment signatures may serve as a first order exploration vector, particularly where erosional windows expose upper level porphyries.

Received 10 June 2025 | Accepted 21 October 2025 | Published 13 November 2025

Introduction

Isotopic systems, including light stable isotopes (*e.g.*, H, O, and S) and radiogenic isotopes (*e.g.*, Pb, Os), have long been used to trace metal sources and understand metal transport processes in ore deposits (*e.g.*, Mathur *et al.*, 2000). However, these systems often offer indirect constraints when compared to the direct application of the metal's own isotopes. Copper, a strongly chalcophile element with two stable isotopes, ^{63}Cu (69.2 %) and ^{65}Cu (30.8 %) (Shields *et al.*, 1965), exists in nature in three oxidation states — Cu^0, Cu^+, and Cu^{2+} (Shields *et al.*, 1965). Following the advent of high precision Cu isotope measurements using MC-ICP-MS (Maréchal *et al.*, 1999), Cu isotopic analysis has become a valuable tool for studying various mineral deposits (*e.g.*, magmatic Ni-Cu sulfide deposits, Ripley *et al.*, 2015; skarn deposits, Maher and Larson, 2007; porphyry Cu deposits, Li *et al.*, 2010). Because porphyry Cu deposits contribute ~75 % of copper resources worldwide they have received the greatest attention from researchers using copper isotopes (Mathur *et al.*, 2009; Li *et al.*, 2010). Significant Cu isotope fractionation has been documented within individual chalcopyrite samples (*e.g.*, Zhu *et al.*, 2000) and between samples from different porphyry Cu deposits (*e.g.*, Li *et al.*, 2010). Factors influencing Cu isotope fractionation include fluid exsolution (Guo *et al.*, 2020), late stage fluid boiling (Rempel *et al.*, 2012), sulfide precipitation (Li *et al.*, 2010), and redox processes (Zhu *et al.*, 2002). However, the majority of these studies have focused on the shallow magmatic-hydrothermal processes that occur within the upper crust or the water-rock interactions that occur during weathering of Cu sulfide-rich rocks in the supergene environment, leaving the deeper processes of magma differentiation largely unexplored.

In the sulfide saturated magmatic systems, the sulfide segregation during magmatic differentiation at mantle conditions has been observed as a key step in producing significant copper isotope fractionation (*e.g.*, Savage *et al.*, 2015; Zhao *et al.*, 2017; Kempton *et al.*, 2022; Liu *et al.*, 2023). The parent magmas of a porphyry Cu deposit system generally contain several hundred to a few thousand ppm S (Richards, 2011). The high sulfur content promotes persistent sulfide saturation during magmatic evolution, distinguishing these systems from barren ones (*e.g.*, Lee and Tang, 2020); consequently early sulfide saturation may serve as an indicator for potential mineralised porphyry. To date, despite its critical role, deep sulfide saturation during lower crustal magma differentiation remains poorly understood because of the rare preservation of representative samples linked to a porphyry Cu ore deposit.

In this study, we investigate Cu isotope variation during deep sulfide accumulation through a valuable collection of amphibole-rich cumulate xenoliths and intermediate-felsic porphyries from the Tongling mining district, China. These samples are unequivocally linked in both time and space to the magmas that formed porphyry Cu deposits, and the mineralised porphyries represent the derivatives of basaltic magmas that underwent sulfide fractionation at mid- to lower-crustal levels (Du and Audétat, 2020). By examining these samples, we aim to shed light on the role of deep sulfide saturation in Cu isotope fractionation and its implications for porphyry Cu deposit formation.

1. School of Earth Science and Resources, Chang'an University, Xi'an 710054, China
2. State Key Laboratory of Geological Processes and Mineral Resources, School of Earth Sciences, China University of Geosciences, Wuhan 430074, China
3. State Key Laboratory of Lithospheric and Environmental Coevolution, School of Earth and Space Sciences, University of Science and Technology of China, Hefei 230026, China
* Corresponding author (e-mail: haihao.guo@cug.edu.cn)

Samples

The Tongling mining district hosts 28 porphyry-skarn Cu (Au, Mo) deposits with a combined resource of ~3.3 Mt Cu and 160 t Au (Fig. S-1; Du and Audétat, 2020). All the ore deposits are hosted by the Early Cretaceous porphyry intrusions composed of pyroxene diorite, granodiorite, and quartz diorite (Fig. S-1; Du and Audétat, 2020). These ore-forming porphyries host abundant amphibole-rich cumulate or megacryst xenoliths. Zircon U-Pb age data indicate that both amphibole-rich xenoliths and the ore-forming porphyries formed at ~140 Ma (Fig. S-2). The investigated samples consist of five amphibole-rich, cumulate xenoliths-porphyry pairs and thirteen mineralised porphyries sampled from three different Early Cretaceous intrusive centres within the Tongling mining district. The amphibole-rich cumulate xenoliths are composed of 70–85 % amphibole, 5–20 % clinopyroxene, and lesser amounts of phlogopite, magnetite, and apatite (Fig. 1); they lack exsolution in the primary mineral phases and typically show little evidence for zoning or secondary melting along the grain boundaries. The cumulate samples show typical accumulate textures and no signs of modal metasomatism, such as veins or presence of interstitial amphibole or mica (Fig. 1). The amphibole-rich cumulate xenoliths contain about 0.1 to ~0.6 vol. % sulfide inclusions but in sample JY-6 no sulfide inclusions are detected. Sulfides are all solitary inclusions with spherical habitats that are enclosed within the primary silicate phases. Early studies show that these sulfide inclusions are dominantly trapped in the form of monosulfide solid solutions (MSS) with Cu contents of 1 to 5.8 wt. % (Du and Audétat, 2020). The studied porphyry assemblage includes two gabbro porphyry, seven pyroxene diorite porphyry, two granodiorite/granodiorite porphyry, six diorite porphyry/quartz diorite, and one granite porphyry samples. Petrographic observations reveal that these samples are generally devoid of late stage sulfide veins and contain neither fluid nor sulfide inclusions within their phenocrysts. However, minor sulfide inclusions are present in sample K6-68, and fluid inclusions are found in JY-6h (Du and Audétat, 2020).

Results

The whole rock and Cu isotope data of amphibole-rich cumulate xenoliths and ore-forming porphyries in this study and other published whole rock data of Tongling ore-forming porphyries are provided in Table S-1. The ore-forming porphyries and cumulates exhibit a calc-alkaline differentiation trend (Fig. S-3). Both the cumulate xenoliths and ore-forming porphyries display geochemical features similar to the arc basalt (Du and Audétat, 2020). The data of silicate melt inclusions revealed that these cumulates crystallised from a basic magma (48–52 wt. % SiO_2; Du and Audétat, 2020). In the Sr/Y *versus* Y and Dy/Yb *versus* SiO_2 diagrams (Fig. S-4a), the magmatic evolution starts in the field of ordinary arc magmas and proceeds into the adakite field, a trend that is indicative of hornblende-dominated fractionation at high pressure (*e.g.*, Loucks, 2014). Hornblende dominated fractionation is also indicated by a negative correlation between Dy/Yb and SiO_2 (Davidson *et al.*, 2007; see Fig. S-4b). Pressure-temperature conditions reconstructed by compositions of amphibole and clinopyroxene within cumulates (Table S-2) show that these cumulates crystallised at 969–1083 °C and 3.8–7.0 kbar (converted to 13–27 km using an

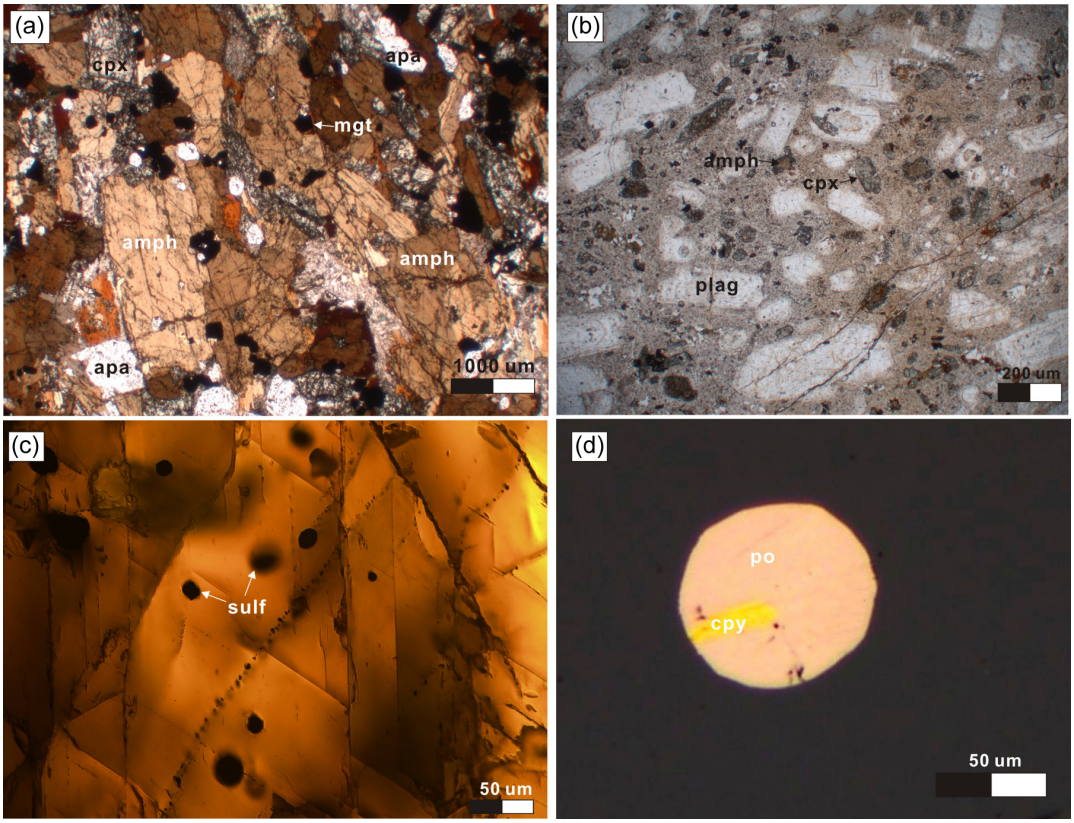

Figure 1 Typical images of cumulates and porphyries from Tongling mining district, southeastern China. **(a)** Amphibole-clinopyroxene cumulate xenolith. **(b)** Thin section of pyroxene diorite porphyry. **(c)** Sulfide inclusions (black) within amphiboles of cumulates. **(d)** Exposed sulfide inclusions comprising of 95 vol. % po and 5 vol. % cpy (po-pyrrhotite, cpy-chalcopyrite, amph-amphibole, cpx-clinopyroxene, apa-apatite, sulf-sulfide). **a**, **b**, and **c** were taken in transmitted light; **d** in reflected light.

average crustal density of 2.7 g cm^{-3}). The mass balance calculation of amphibole dominated fractionation yielded a good fit between estimated and actual residual melt (Table S-3). These lines of evidence, combined with the consistent crystallisation age of cumulates to ore-forming porphyries (Fig. S-2), strongly suggests that the ore-forming magmas in the Tongling mining district experienced significant clinopyroxene and amphibole fractionation at mid- to lower-crustal levels.

Copper isotopic analyses were performed by a sample standard bracketing method with purification using ion chromatography (BioRad AG-MP-1M strong anion resin) on a Thermo Scientific Neptune Plus MC-ICP-MS at University of Science and Technology of China (USTC). The long term external precision of δ^{65}Cu data is better than 0.05 ‰ (2 s.d.) (details in Supplementary Information). The Cu isotopic ratios of these rocks display correlations with their Cu contents and indicators of magmatic differentiation such as SiO_2, MgO, FeO^t, and Al_2O_3 abundances (respectively $r^2 = 0.37$, 0.55, 0.51 and 0.67; Fig. 2). The sulfide-bearing amphibole-rich cumulate xenoliths generally have high Cu contents of 87 to 528 ppm (average value = 26 ppm, $n = 4$) and light Cu isotopic compositions with δ^{65} Cu values ranging from –0.25 ‰ to –0.17 ‰ except one sulfide-free sample JY-6 (Cu content of 77 ppm, δ^{65}Cu = 0.58 ‰). The ore-forming porphyries have lower Cu contents of 17 to 201 ppm (average value = 55 ppm, $n = 17$) and higher δ^{65}Cu values of –0.04 ‰ to 0.37 ‰ (average value = 0.27 ‰, $n = 16$) except the outlier of sulfide-bearing sample K6-68, with an apparently lower δ^{65} Cu value of –0.24 ‰. The porphyry sample JY-6h hosts higher Cu contents than other porphyries, possibly caused by the fluid inclusions within its phenocryst.

Discussion

The copper isotope compositions of our data are systematically divided into two groups: the sulfide saturated cumulates with negative δ^{65}Cu values; the porphyries with positive δ^{65}Cu values. Below we explore the possible causes for the copper isotope variations including (1) fluid saturation and exsolution, (2) redox effects, (3) mantle metasomatism, and (4) fractional crystallisation and sulfide segregation.

Partitioning of Cu isotopes between hydrothermal fluids and precipitating Cu sulfides could generate significant Cu isotope fractionation (up to 1.2 ‰) (*e.g.*, Li *et al.*, 2010). The fresh nature of the analysed samples and the absence of fluid inclusions within the phenocrysts exclude this interference. Redox related Cu isotope fractionation processes have played an important role in generating the high δ^{65}Cu signatures (*e.g.*, Zhu *et al.*, 2002) because Cu^{2+} species preferentially incorporate heavier isotopes which have shorter, stronger bonds compared to Cu^{+} species (*e.g.*, Markl *et al.*, 2006). Liu *et al.* (2015) have observed significant Cu isotope variation (from −0.64 to 1.82 ‰) during oxidative dissolution of sulfides. The encapsulation of sulfide inclusions within silicate minerals and the absence of magnetite in these inclusions indicate minimal oxidation occurs (Fig. 1). Mantle metasomatism is treated as another predominant control on the isotopic variation. This process involves fluids derived from the recycled ocean-crustal material interaction with the mantle xenoliths that formed by fractional crystallisation of basalts (Liu *et al.*, 2015; Kempton *et al.*, 2022). The hornblendites in our study have a typical mechanical cumulate origin, that is greatly different from those metasomatic mantle xenoliths which often display a poikilitic texture and host interstitial sulfide grains or veins (*e.g.*, Kempton *et al.*, 2022).

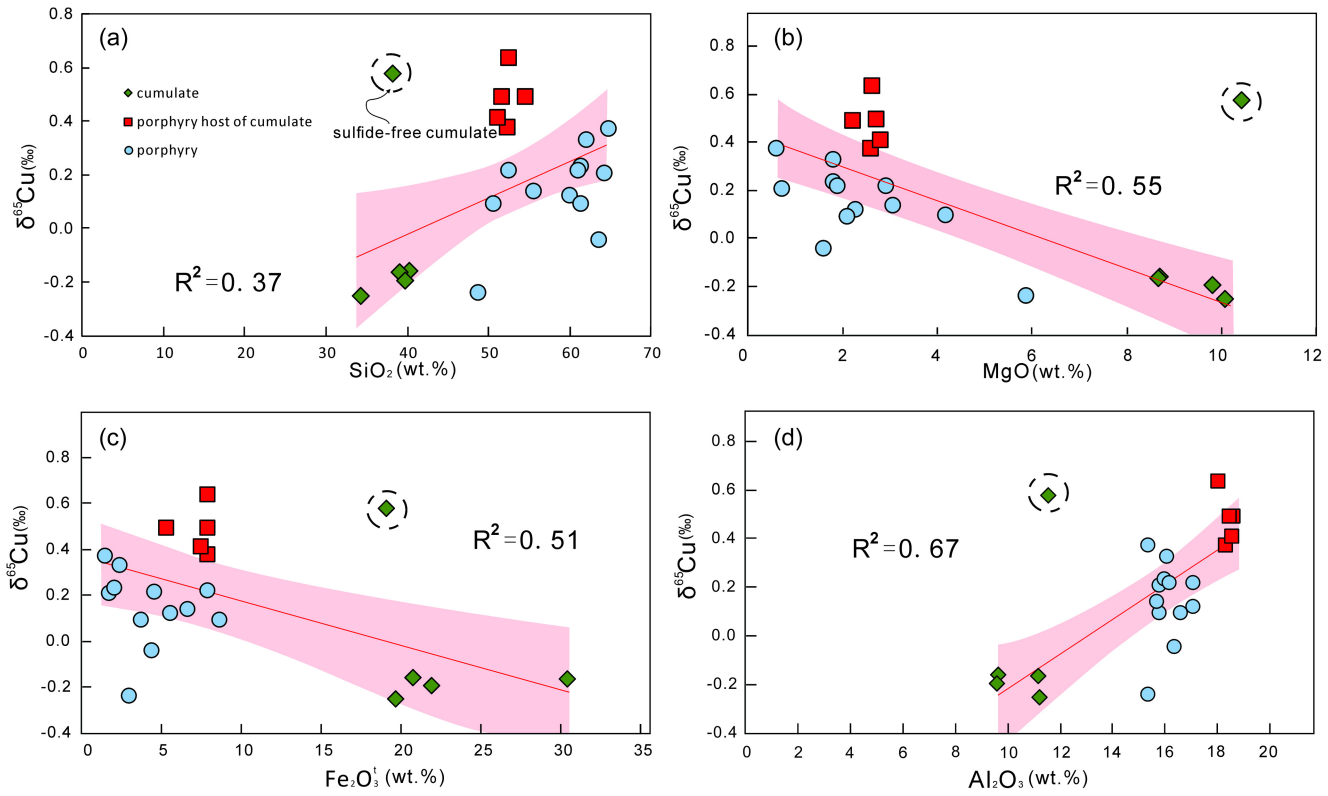

Figure 2 The correlation between δ^{65}Cu and whole rock **(a)** SiO_2, **(b)** MgO, **(c)** $Fe_2O_3^t$, and **(d)** Al_2O_3 contents. Overall, the δ^{65}Cu of the cumulates and ore-forming porphyries shows an increasing tendency with magmatic differentiation, though the porphyry hosts of cumulates do not match well with the quantitative relationship. The δ^{65}Cu of cumulates samples shows a stable range with magmatic fractionation.

The correlation between $\delta^{65}Cu$ and magmatic differentiation indicators such as SiO_2, MgO, FeO^t, and Al_2O_3 abundances (respectively $r^2 = 0.37$, 0.55, 0.51 and 0.67; Fig. 2) highlights the major role of magmatic processes. Our data show that mineral phases like clinopyroxene and amphibole in the studied cumulates have low Cu budgets (*e.g.*, 1.4–3.3 ppm; Table S-4). Consequently, their crystallisation is unlikely to cause substantial Cu isotope fractionation and cannot account for the high Cu budgets (87–528 ppm) of the bulk cumulates. Fe-Ti oxides, also analysed from these cumulates, contain negligible Cu (~0.54 ppm; Table S-4). In contrast, sulfide inclusions contain 1.1–5.8 wt. % Cu, contributing ~100–500 ppm to whole rock budgets and dominating the Cu inventory. Experimental studies indicate sulfide melts preferentially incorporate light Cu compared to coexisting silicate melts ($\Delta^{65}Cu_{sulfide-silicate} \leq 0$; Fig. 3; Savage *et al.*, 2015). It is also noted that the variation of Ni content in sulfides from ~25–27 wt. % to 1 wt. % could generate Cu isotopic fractionation (Xia *et al.*, 2019; Ni *et al.*, 2024). The narrow range of Cu isotopic compositions, along with low Ni content (<0.1 wt. %) in sulfide inclusions of cumulates (Du and Audétat, 2020), indicates rapid sulfide formation, justifying the modelling of the entire cumulate as a single unit. Therefore, the measured bulk rock $\delta^{65}Cu$ variations of these cumulates should reflect the integrated composition of the sulfide inclusions and the shift in Cu isotope composition likely results from sulfide segregation from the melt. In the sulfide saturated (Ripley *et al.*, 2015; Zhao *et al.*, 2017; Liu *et al.*, 2023) magmatic system, sulfide segregation from basaltic magmas could result in the residual melt being more enriched in $\delta^{65}Cu$ (Fig. 3). Therefore, the isotopically light Cu cumulate segregation will generate an isotopically heavy upper continental crust (Liu *et al.*, 2023).

To better understand the effect of sulfide segregation during fractional crystallisation on the variation of Cu isotopic compositions, we conducted simulations using the Rayleigh fractionation equations as follows in Equations (1) to (3):

$$C_{silicate\ melt} = C_0 * F^{(D-1)} \quad \text{Eq. 1}$$

$$\delta^{65}Cu_{silicate\ melt} = (\delta^{65}Cu_0 + 1000) * f^{(\alpha-1)} - 1000 \quad \text{Eq. 2}$$

$$\delta^{65}Cu_{cumulate} = (\delta^{65}Cu_0 + 1000) * (1 - f^{\alpha})/(1 - f) - 1000 \quad \text{Eq. 3}$$

where α represents the equilibrium Cu isotope fractionation factor between sulfide and the residual silicate melt; C_0 and $C_{silicate\ melt}$ are element concentrations of the initial and the evolving silicate melts; D is the partitioning coefficient of Cu between cumulate and silicate melt; F denotes the mass fraction of the evolving silicate melt. The fraction of Cu remaining in the residual melt (f) is calculated by $f = (1 - F) * (C_{silicate\ melt}/C_0)$, assuming an initial Cu content of ~60 ppm, typical of primary continental arc basalts, and a $\delta^{65}Cu$ of 0.06 ‰, consistent with the Bulk Silicate Earth (see Fig. 3; Liu *et al.*, 2015). Choosing different initial Cu or $\delta^{65}Cu$ values in the model may lead to different $\delta^{65}Cu$ values for the predicted melts but would not change the relative $\delta^{65}Cu$ variation between the parental melts and evolving melts. The $\alpha_{sulfide\ melt\text{-}silicate\ melt}$ is assumed to remain constant during magmatic differentiation. Because of the insignificant Cu content in silicates and oxides, $\alpha_{sulfide\ melt\text{-}silicate\ melt}$ is approximately equal to $\alpha_{cumulates\text{-}silicate\ melt}$. These cumulates have crystallisation temperatures (969–1083 °C), pressures (3.8–7.0 kbar) and oxygen fugacities of ΔFMQ +0.7 to +1.3 (Table S-2). Under these conditions and Ni-poor sulfides, the Cu^+ dominates in the silicate melt and sulfide melt and the

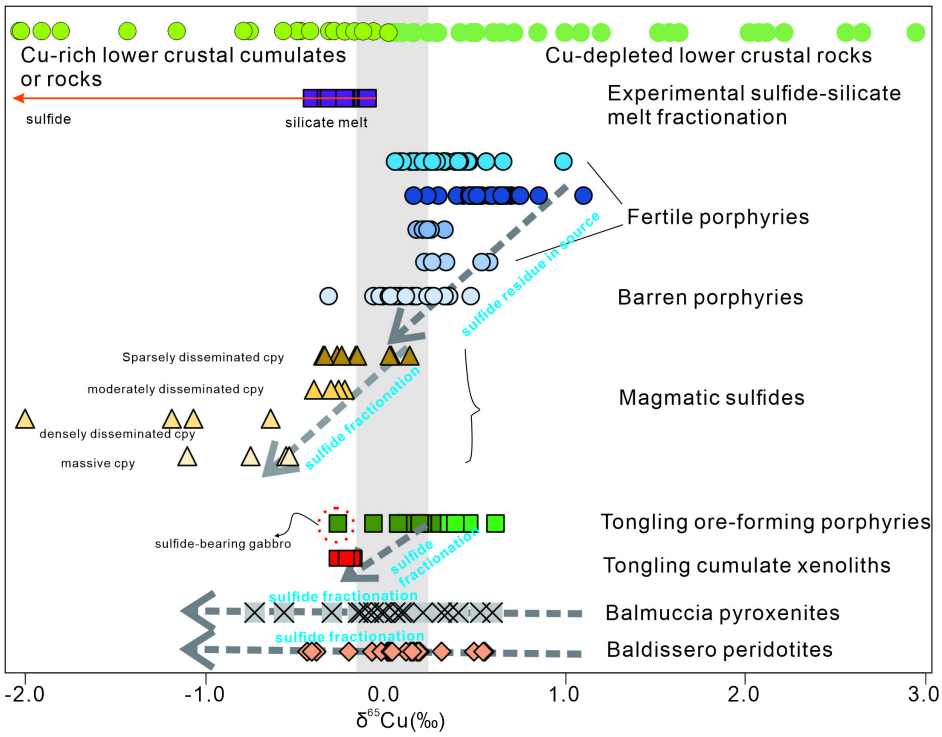

Figure 3 Copper isotopes of ore-forming porphyries and sulfide-bearing cumulate xenoliths in Tongling ore district compared with other sulfide saturated magmatic systems worldwide. Data sources as follows: fertile and barren porphyries in the porphyry Cu system (Zheng *et al.*, 2019); sparsely/moderately/densely/massive chalcopyrite (cpy) in a magmatic sulfide ore system (Zhao *et al.*, 2017); sulfide saturated mantle peridotites or pyroxenites (Huang *et al.*, 2017; Zou *et al.*, 2019). The equilibrium Cu isotope fractionation between sulfide and silicate melts is from the experimental work of Xia *et al.* (2019); Cu-rich lower crustal cumulate or rocks and Cu-depleted lower crustal rocks (Liu *et al.*, 2023 and references therein). Noting that sulfide segregation (or the residue in the source) will consistently enrich the differentiated melt in $\delta^{65}Cu$. Gray band represents the range for Bulk Silicate Earth from Liu *et al.* (2015).

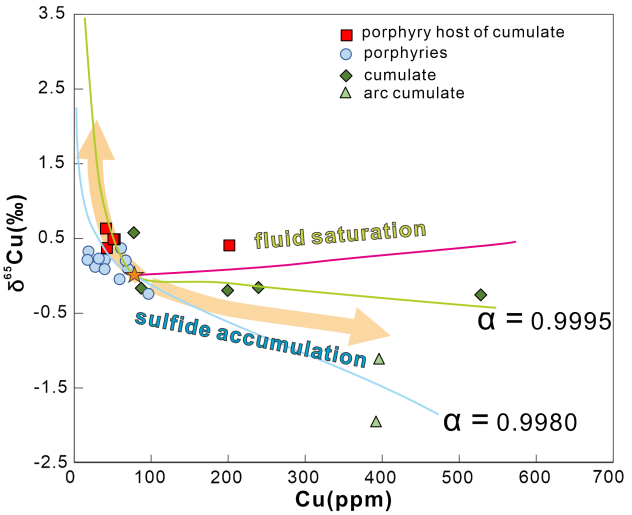

Figure 4 The correlation between δ^{65}Cu and Cu content for cumulates and ore-forming porphyries at Tongling mining district. After sulfide segregation in the cumulates, the ore-forming porphyries obviously move towards more Cu depletion and a heavy copper isotopic trend. In the modelling, the initial melt (star) has ~60 ppm Cu and Cu isotopic composition (δ^{65}Cu) of 0.06 ‰ equal to that of the BSE (Liu *et al.*, 2015); the *D* value is 8, assuming sulfide fraction is 0.01 and $D_{sulfide/melt}$ = 800 (Lee *et al.*, 2012). The δ^{65}Cu and Cu content of arc cumulates are collected from Liu *et al.* (2023). The pink line represents the modelling of fluid saturation process as described in Guo *et al.* (2020).

corresponded equilibrium Cu isotope fractionation factors ($\alpha_{sulfide-silicate\ melt}$) are ~0.9995 to 0.9980 (Xia *et al.*, 2019). It is obvious that the sulfide-bearing cumulates tend to show lower δ^{65}Cu relative to the initial basaltic melt and the differentiated magmas show higher δ^{65}Cu (Fig. 4). Though the model makes little difference to the overall δ^{65}Cu enrichment trend caused by sulfide segregation during magmatic differentiation, with one fluid inclusion-bearing sample deviating (sample JY-6h).

Geological Implications

Porphyry Cu (Au, Mo) deposits are typically hosted in rocks ranging from intermediate to felsic compositions, which have undergone a range of geological processes from the mantle source to the surface (Sillitoe, 2010). During partial melting of the mantle, copper isotopes are essentially unfractionated, with the copper isotopic compositions of basaltic magma or mantle rocks closely aligning with values representative of the Bulk Silicate Earth (−0.14 to ~+ 0.20 ‰; Savage *et al.*, 2015; Liu *et al.*, 2015). As the basaltic magmas stagnate at or near the crust-mantle boundary, deep crustal differentiation processes facilitate a substantial loss of metals from the magma to crystallising cumulate sulfides (Du and Audétat, 2020). This process is pivotal in imprinting heavy copper isotopic signatures onto evolved, intermediate composition porphyries (Fig. S-5). As derivative intermediate magmas ascend to shallow depths (5–15 km), fluid saturation and exsolution occur (Fig. S-5). The exsolved fluid phases are enriched in heavy Cu isotopes (^{65}Cu) relative to the coexisting silicates (Fig. 4; Guo *et al.*, 2020), continuous migration of low density hydrothermal fluids from the mineralisation centre leads to a systematic increase in Cu isotope ratios from centre outward (Li *et al.*, 2010; Mathur *et al.*, 2009). This overall Cu isotopic evolution of porphyry Cu ore deposit leads to a continuous increase in Cu isotopic signatures from the source to the final deposition site. The porphyry rocks with elevated concentrations of heavier copper isotopes should identify potential porphyry Cu orebodies. This assertion is supported by the findings of Zheng *et al.* (2019), who have shown that many fertile porphyries show heavier copper isotopes than barren ones. On the premise that Cu isotope behaviour is well estimated in the weathering processes, the heavy Cu signature may be an exploration vector in detrital materials or downstream of a porphyry.

Acknowledgements

This study was supported financially by the National Key R & D Program of China [2023YFF0804200 and 2023YFF0806400], the National Natural Science Foundation of China [grants 42002072 and 42373038], Natural Science Basic Research Program of Shaanxi [Program No. 2023-JC-QN-0336], and Hubei Provincial Natural Science Foundation of China [No. 2025AFA005]. We thank Jian Huang for his comments on the study. We are grateful to Paul Savage and three anonymous reviewers for constructive remarks, and the editor Ambre Luguet for handing this manuscript.

Editor: Ambre Luguet

Additional Information

Supplementary Information accompanies this letter at https://www.geochemicalperspectivesletters.org/article2545.

Cite this letter as: Du, J., Guo, H., Fang, S., Huang, F. (2025) Copper isotope fractionation during lower crustal sulfide accumulation. *Geochem. Persp. Let.* 37, 45–50. https://doi.org/10.7185/geochemlet.2545

References

Davidson, J., Turner, S., Handley, H., Macpherson, C., Dosseto, A. (2007) Amphibole "sponge" in arc crust? *Geology* 35, 787–790. https://doi.org/10.1130/G23637A.1

Du, J.G., Audétat, A. (2020) Early sulfide saturation is not detrimental to porphyry Cu-Au formation. *Geology* 48, 519–524. https://doi.org/10.1130/G47169.1

Guo, H.H., Xia, Y., Bai, R.X., Zhang, X.C., Huang, F. (2020) Experiments on Cu-isotope fractionation between chlorine-bearing fluid and silicate magma: implications for fluid exsolution and porphyry Cu deposits. *National Science Review* 7, 1319–1330. https://doi.org/10.1093/nsr/nwz221

Huang, J., Huang, F., Wang, Z.C., Zhang, X.C., Yu, H.M. (2017) Copper isotope fractionation during partial melting and melt percolation in the upper mantle: Evidence from massif peridotites in Ivrea-Verbano Zone, Italian Alps. *Geochimica et Cosmochimica Acta* 211, 48–63. https://doi.org/10.1016/j.gca.2017.05.007.

Kempton, P.D., Mathur, R., Harmon, R.S., Bell, A., Hoefs, J., Shaulis, B. (2022) Cu-Isotope Evidence for Subduction Modification of Lithospheric Mantle. *Geochemistry, Geophysics, Geosystems* 23, e2022GC010436. https://doi.org/10.1029/2022GC010436

Lee, C.-T.A., Tang, M. (2020) How to make porphyry copper deposits. *Earth and Planetary Science Letters* 529, 115868. https://doi.org/10.1016/j.epsl.2019.115868

Lee, C.-T.A., Luffi, P., Chin, E.J., Bouchet, R., Dasgupta, R., Morton, D.M., Le Roux, V., Xin, Q.Z., Jin, D. (2012) Copper systematics in arc magmas and implications for crust-mantle differentiation. *Science* 336, 64–68. https://doi.org/10.1126/science.1217313

Li, W.Q., Jackson, S.E., Pearson, N.J., Graham, S. (2010) Copper isotopic zonation in the Northparkes porphyry Cu–Au deposit, SE Australia. *Geochimica et Cosmochimica Acta* 74, 4078–4096. https://doi.org/10.1016/j.gca.2010.04.003

Liu, S.A., Huang, J., Liu, J., Wörner, G., Yang, W., Tang, Y.J., Chen, Y., Tang, L., Zheng, J., Li, S. (2015) Copper isotopic composition of the silicate Earth. *Earth and Planetary Science Letters* 427, 95–103. https://doi.org/10.1016/j.epsl.2015.06.061

Liu, S.A., Rudnick, R.L., Liu, W.R., Teng, F.Z., Wu, T.H., Wang, Z.Z. (2023) Copper isotope evidence for sulfide fractionation and lower crustal foundering in making continental crust. *Science Advances* 9, eadg6995. https://doi.org/10.1126/sciadv.adg6995

Loucks, R.R. (2014) Distinctive composition of copper-ore-forming arc magmas. *Australian Journal of Earth Sciences* 61, 5–16 https://doi.org/10.1080/08120099.2013.865676

Maher, K.C., Larson, P.B. (2007) Variation in copper isotope ratios and controls on fractionation in hypogene skarn mineralization at Coroccohuayco and Tintaya, Peru. *Economic Geology* 102, 225–237. https://doi.org/10.2113/gsecongeo.102.2.225

Maréchal, C.N., Télouk, P., Albarède, F. (1999) Precise analysis of copper and zinc isotopic compositions by plasma-source mass spectrometry. *Chemical Geology* 156, 251–273. https://doi.org/10.1016/S0009-2541(98)00191-0

Markl, G., Lahaye, Y., Schwinn, G. (2006) Copper isotopes as monitors of redox processes in hydrothermal mineralization. *Geochimica et Cosmochimica Acta* 70, 4215–4228. https://doi.org/10.1016/j.gca.2006.06.1369

Mathur, R., Ruiz, J., Titley, S., Gibbins, S., Margotomo, W. (2000) Different crustal sources for Au-rich and Au-poor ores of the Grasberg Cu-Au porphyry deposit. *Earth and Planetary Science Letters* 183, 7–14. https://doi.org/10.1016/S0012-821X(00)00256-9

Mathur, R., Titley, S., Barra, F., Brantley, S., Wilson, M., Phillips, A., Munizaga, F., Maksaev, V., Vervoort, J., Hart, G. (2009) Exploration potential of Cu isotope fractionation in porphyry copper deposits. *Journal of Geochemical Exploration* 102, 1–6. https://doi.org/10.1016/j.gexplo.2008.09.004

Ni, P., Zhan, Y., Chabot, N.L., Ryan, C.J., Zhu, K., Nie, N.X., Shirey, S.B., Shahar, A. (2024) Copper isotope fractionation during asteroid core solidification. *Geochemical Perspectives Letters* 31, 49–53. https://doi.org/10.7185/geochemlet.2432

Rempel, K.U., Liebscher, A., Meixner, A., Romer, R.L., Heinrich, W. (2012) An experimental study of the elemental and isotopic fractionation of copper between aqueous vapour and liquid to 450°C and 400 bar in the CuCl–NaCl–H_2O and CuCl–NaHS–NaCl–H_2O systems. *Geochimica et Cosmochimica Acta* 94, 199–216. https://doi.org/10.1016/j.gca.2012.06.028

Richards, J.P. (2011) High Sr/Y arc magmas and porphyry Cu ± Mo ± Au deposits: just add water. *Economic Geology* 106, 1075–1081. https://doi.org/10.1016/j.oregeorev.2011.05.006

Ripley, E.M., Dong, S.F., Li, C.S., Wasylenki, L.E. (2015) Cu isotope variations between conduit and sheet-style Ni-Cu-PGE sulfide mineralization in the Midcontinent Rift System, North America. *Chemical Geology* 414, 59–68. https://doi.org/10.1016/j.chemgeo.2015.09.007

Savage, P.S., Moynier, F., Chen, H., Shofner, G., Siebert, J., Badro, J., Puchtel, I.S. (2015) Copper isotope evidence for large-scale sulphide fractionation during Earth's differentiation. *Geochemical Perspectives Letters* 1, 53–64. https://doi.org/10.7185/geochemlet.1506

Shields, W.R., Goldich, S.S., Garner, E.L., Murphy, T.J. (1965) Natural variations in the abundance ratios and the atomic weight of copper. *Journal of Geophysical Research* 70, 479–491. https://doi.org/10.1029/JZ070i002p00479

Sillitoe, R.H. (2010) Porphyry copper systems. *Economic Geology* 105, 3–41. https://doi.org/10.2113/gsecongeo.105.1.3

Xia, Y., Kiseeva, E.S., Wade, J., Huang, F. (2019) The effect of core segregation on the Cu and Zn isotope composition of the silicate Moon. *Geochemical Perspectives Letters* 12, 12–17. https://doi.org/10.7185/geochemlet.1928

Zhao, Y., Xue, C.J., Liu, S.A., Symons, D.T.A., Zhao, X.B., Yang, Y.Q., Ke, J.J. (2017) Copper isotope fractionation during sulfide-magma differentiation in the Tulaergen magmatic Ni–Cu deposit, NW China. *Lithos* 286–287, 206–215. http://dx.doi.org/10.1016/j.lithos.2017.06.007

Zheng, Y.C., Liu, S.A., Wu, C.D., Griffin, W.L., Li, Z.Q., Xu, B., Yang, Z.M., Hou, Z.Q., O'Reilly, S.Y. (2019) Cu isotopes reveal initial Cu enrichment in sources of giant porphyry deposits in a collisional setting. *Geology* 47, 135–138. https://doi.org/10.1130/G45362.1

Zhu, X.K., O'Nions, R.K., Guo, Y., Belshaw, N.S., Rickard, D. (2000) Determination of natural Cu-isotope variation by plasma-source mass spectrometry: Implications for use as geochemical tracers. *Chemical Geology* 163, 139–149. https://doi.org/10.1016/S0009-2541(99)00076-5

Zhu, X.K., Guo, Y., Williams, R.J.P., O'Nions, R.K., Matthews, A., Belshaw, N.S., Canters, G.W., de Waal, E.C., Weser, U., Burgess, B.K., Salvato, B. (2002) Mass fractionation processes of transition metal isotopes. *Earth and Planetary Science Letters* 200, 47–62. https://doi.org/10.1016/S0012-821X(02)00615-5

Zou, Z., Wang, Z., Li, M., Becker, H., Geng, X., Hu, Z., Lazarov, M. (2019) Copper isotope variations during magmatic migration in the mantle: Insights from mantle pyroxenites in Balmuccia peridotite massif. *Journal of Geophysical Research: Solid Earth* 124, 11130–11149. https://doi.org/10.1029/2019JB017990

Geochemical Perspectives Letters

Copper isotope fractionation during lower crustal sulfide accumulation

J. Du, H. Guo, S. Fang, F. Huang

Supplementary Information

The Supplementary Information includes:

- Methods
- Tables S-1 to S-4
- Figures S-1 to S-5
- Supplementary Information References

Methods

Whole-rock major and trace elements

Major-element compositions were determined by X-ray fluorescence using an XRF-1800 spectrometer at Beijing Createch Testing Technology Co., Ltd., Beijing, China. Samples were fused in a $Li_2B_4O_7$ flux (sample:flux = 1:5) at temperatures of 1150-1250 °C, and formed into glass discs for analysis. Loss on ignition (LOI) values were obtained from 2 g of powdered sample after 1 h of calcination at 1100 °C. Accuracy was better than ± 3 %. Trace-element and rare-earth element (REE) compositions were determined by ICP-MS using a Agilent 7500 spectrometer at Beijing Createch Testing Technology Co., Ltd., Beijing, China. About 50 mg of pulverized sample was placed in a sealed Teflon beaker and digested with HF + HNO_3 for 2-3 days before $HClO_4$ was added for further digestion. After evaporation to dryness, 5 % HNO_3 solution was added to a volume of 50 mL for analysis. Rock standards of the GBW series were analysed together with samples to check reproducibility. Precision was estimated to be better than ±10 %. Rh was used as an internal standard. USGS rock standards GSP-1 and AGV-2 were chosen for calibration of the procedure. Analytical uncertainties were better than ± 5 % for most trace elements.

Copper isotopes analyses

Copper isotopic analyses were performed at the Metal Stable Isotope Laboratory of the University of Science and Technology of China (USTC). Rock powders were dissolved in Savillex beakers with caps using double-distilled concentrated HF+HNO_3, HCl + HNO_3 and HCl. The fully digested samples were taken up in 1 ml 6 N HCl + 0.001 % H_2O_2 for ion chromatography with BioRad AG-MP-1M strong anion resin. After the sample was loaded onto the column in 1 ml of 6 N HCl + 0.001 % H_2O_2, matrix elements were then eluted with 5 ml of 6 N HCl + 0.001 % H_2O_2. The column chemistry was performed twice, and then matrix elements of Na, Ti, Fe, Mg, and Al were checked for each eluted Cu fractions using ICP-MS. The whole procedure can be repeated if further purification is required. Copper yields were >99.5 %, and total procedural Cu blanks

(from sample dissolution to mass spectrometry) were 0.65 ng, insignificant relative to the amounts of Cu (1-10 µg) onto columns. The isotopic analyses were performed by a sample standard bracketing method on a Thermo Scientific Neptune Plus MC–ICP–MS at low-resolution mode. The purified samples were dissolved in 2 % HNO_3 and introduced into the instrument using an ESI PFA microflow nebulizer with an uptake rate of (50 µL·min–1 flow rate). ^{63}Cu and ^{65}Cu isotope beams were collected in C and L2 faraday cups, respectively. Ni and Zn were monitored using ^{62}Ni and ^{64}Zn beams in L3 and L1 in the same cup setup. The $\delta^{65}Cu$ of each sample is the average of 3 analyses, and the average is reported. Copper isotope data are reported in the standard notation in per mil relative to the standard reference material NIST 976: $\delta^{65}Cu = [(^{65}Cu/^{63}Cu)_{sample}/(^{65}Cu/^{63}Cu)_{NIST\ 976} -1] \times 1000$ ‰. Repeated analyses of two mono-element reference materials yield δ^{65} Cu of 0.19 ± 0.05 ‰ (2SD, n = 1026) for ERM-AE-647 and 0.31 ± 0.05 ‰ (2SD, n = 611) for AAS. The long-term external precision of $\delta^{65}Cu$ of our data is better than 0.05 ‰ (2SD, 95% confidence interval).

Electron probe micro-analysis

The major element chemistry of clinopyroxene and amphibole from cumulates was determined at China University of Geosciences, Beijing, China, using a Superprobe 733-type electron microprobe operated at an accelerating voltage of 15 kV, beam current of 20 nA, and beam size of 5 μ m. Natural and synthetic minerals and alloys were used as standards. The microprobe was calibrated using standards of quartz, rutile, plagioclase, chromite, almandine, rhodonite, calcite, albite, apatite, CoO, and NiO. The detection time for most elements was 100 s, and analytical error was ± 2 %.

Laser Ablation Inductively Coupled Plasma Mass Spectrometer analysis

In situ trace element analysis of amphibole, clinopyroxene and magnetite in cumulates was undertaken at the Laboratory of Mineralization and Dynamics, Chang'an University, Xi'an, China, using an Agilent 7700x ICP-MS and a Photo Machines Analyte Excite 193 nm LA system. Helium was used as a carrier gas to enhance the transport efficiency of the ablated material. Argon was used as the make-up gas and mixed with the carrier gas via a T-connector before entering the ICP-MS. The LA was performed using a beam diameter of 35 µm, a frequency of 6 Hz, and an energy density of 4.5 J/cm^2. For the silicate minerals (amphibole and clinopyroxene), each analysis included background acquisition of 20 s (gas blank) followed by 45 s of data acquisition during laser ablation. NIST 610, NIST612, BHVO-2G, BCR-2G, and BIR-1G were analyzed after every 10 mineral analyses. Offline data selection and integration of background and analyte signals, time drift corrections, and quantitative calibrations of the trace element analyses were conducted using ICPMSDataCal software (Liu *et al*., 2008), with Si as the internal standard and NIST 610, NIST 612, BHVO-2G, BCR-2G, and BIR-1G as the external standards. For the magnetite, each analysis included a 20 s background acquisition and a 40 s data acquisition during laser ablation. NIST 610, NIST612, GSE-1G, BHVO-2G, BCR-1G and BCR-2G were analyzed after every 10 mineral analyses. Offline data selection and integration of background and analyte signals, time drift corrections, and quantitative calibrations of the trace element analyses of magnetite were conducted using multiple external standards (GSE-1G, BHVO-2G, BCR-1G and BCR-2G) as standards without an internal standard in the ICPMSDataCal software (Liu *et al*., 2008).

P-T-fO_2 conditions of magma crystallization

The following methods were applied to estimate the P-T-fO_2 conditions of magma crystallization: (1) Clinopyroxene - liquid thermobarometry (Neave and Putirka, 2017), (2) Amphibole - liquid thermobarometry (Putirka, 2016), and (3) Amphibole oxybarometry (Ridolfi *et al*. 2010). For clinopyroxene-liquid thermobarometry we used the approach described in Neave and Putirka (2017), utilizing the spreadsheet provided with that study. However, whereas Neave and Putirka (2017) tested in their case study all individual whole-rock compositions to identify the best-matching liquid composition (defined by an equilibrium iron-magnesium exchange coefficient ($K_{D(Fe\text{-}Mg)}$) of 0.27 ± 0.03), we related all elements numerically to SiO_2 based on fitting equations in Harker diagrams, and then SiO_2 was varied via goal seek until an equilibrium

$K_{D(Fe\text{-}Mg)}$ value is found. Mineral compositions for which no matching liquid composition could be found using this constraint were discarded. The clinopyroxene-liquid thermobarometer was calibrated to an uncertainty of ± 1.4 kbar and ca. ± 30 °C (Putirka, 2008; Neave and Putirka, 2017). For the calculations we assumed a melt H_2O content of 5 wt. %. Varying this value by ± 2 wt. % H_2O results in a temperature change of ± 25 °C and a pressure change of ±0.3 kbar.

For amphibole-liquid thermobarometry, we used the spreadsheet provided by Putirka (2016). As a first step, a pressure- and liquid-independent temperature is calculated, and this temperature is then used in conjunction with potential liquid compositions and an equilibrium $K_{D(Fe\text{-}Mg)}$ value of 0.28±0.11 to calculate pressure. Again, whole-rock compositions were numerically related to SiO_2, and SiO_2 was then varied via goal seek until an equilibrium $K_{D(Fe\text{-}Mg)}$ value was found. Amphibole compositions for which no equilibrium liquid composition could be found were discarded. This thermobarometer is associated with an uncertainty of ±2-4 kbar and ca.±30 °C (Putirka, 2016). However, while the calculated temperatures are robust, the calculated pressures depend strongly on melt H_2O content, which was again set to 5 wt. %. Changing this value by ±2 wt. % H_2O results in a pressure change of ± 0.8-1.3 kbar.

For amphibole oxybarometry, we used the spreadsheet provided by Ridolfi *et al*. (2010). At the first step, only amphiboles that pass through the equilibrium test by amphibole-liquid thermobarometry were further taken to estimate the oxygen fugacity. The amphibole oxybarometer has an uncertainty of ± 0.4–0.8 ΔFMQ (i.e., relative to the fayalite-magnetite-quartz buffer) and was little affected by temperature, pressure, and melt composition.

Supplementary Tables

Table S-1 Whole-rock (major oxides in wt. %, trace elements in ppm) and copper isotopic data of amphibole-rich cumulates and intermediate porphyries at Tongling.

Samples	Rock type	$\delta^{65}Cu$	2SD	SiO_2	TiO_2	Al_2O_3	Fe_2O_3t	MgO	MnO	CaO	Na_2O	K_2O	P_2O_5
XTJ-14	granodiorite	-0.04	0.05	63.7	0.6	16.4	4.4	1.6	0.1	4.7	4.1	3.0	0.2
CS01	pyroxene diorite	0.09	0.02	50.6	1.2	15.8	8.6	4.2	0.2	10.3	3.6	2.6	0.6
K6-68	gabbro porphyry	-0.24	0.03	48.9	1.3	15.3	3.0	5.9	0.2	9.1	3.6	3.2	0.7
STJ02	granodiorite porphyry	0.37	0.04	64.8	0.4	15.4	1.5	0.6	0.0	3.9	4.6	2.9	0.2
QTY03	granite porphyry	0.21	0.03	64.3	0.4	15.8	1.7	0.7	0.0	4.0	4.3	4.9	0.2
MJ01	pyroxene diorite	0.14	0.01	55.6	0.8	15.7	6.6	3.1	0.1	5.3	4.1	3.0	0.4
DLC01	diorite porphyry	0.12	0.04	60.1	0.6	17.1	5.6	2.3	0.1	3.7	5.1	2.8	0.2
MLT02	gabbro	0.22	0.04	52.5	1.1	17.1	7.9	2.9	0.2	7.6	4.2	3.1	0.5
JC-019	diorite porphyry	0.23	0.01	61.4	0.6	16.0	2.1	1.8	0.1	6.8	4.0	3.9	0.3
JC-018	diorite porphyry	0.33	0.03	62.0	0.6	16.1	2.4	1.8	0.1	6.5	3.3	4.1	0.3
SK3402	diorite porphyry	0.21	0.02	61.1	0.7	16.2	4.6	1.9	0.1	5.1	2.7	4.2	0.3
JC-012	diorite porphyry	0.09	0.03	61.4	0.7	16.6	3.7	2.1	0.1	5.6	3.4	3.5	0.3
JY-2h	pyrite diorite porphyry	0.64	0.01	52.6	1.2	18.0	7.9	2.6	0.2	8.7	4.9	2.8	0.5
JY-3h	pyrite diorite porphyry	0.37	0.03	52.4	1.2	18.3	7.9	2.6	0.2	8.6	4.9	2.8	0.5
JY-4h	pyrite diorite porphyry	0.49	0.01	54.5	1.1	18.6	5.3	2.2	0.1	10.1	5.8	0.6	0.4
JY-5h	pyrite diorite porphyry	0.49	0.03	51.7	1.2	18.5	7.9	2.7	0.2	8.8	4.9	2.9	0.5
JY-6h	pyrite diorite porphyry	0.41	0.03	51.2	1.3	18.5	7.5	2.8	0.2	8.9	4.6	3.6	0.5
JY-2	cumulate	-0.16	0.02	40.3	2.5	9.6	20.8	8.7	0.3	14.0	1.7	1.0	2.1
JY-3	cumulate	-0.17	0.02	39.1	3.7	11.2	30.4	8.7	0.3	10.5	1.6	1.3	1.5
JY-4	cumulate	-0.25	0.01	34.3	2.8	11.2	19.7	10.1	0.2	15.0	1.7	1.5	2.0
JY-5	cumulate	-0.20	0.03	39.8	3.0	9.6	21.9	9.8	0.2	14.6	1.6	1.0	3.5
JY-6	cumulate	0.58	0.04	38.2	2.9	11.6	19.1	10.4	0.2	15.7	1.7	1.5	2.2

Table S-1 continued

Samples	Li	Be	Sc	V	Cr	Co	Ni	Cu	Zn	Ga	As	Rb	Sr	Y	Zr	Nb	Cs	Ba
XTJ-14	7.8	2.4	8.6	88	7.4	9.7	3.8	59	47	23.6	N/A	116	778	22	27	14	2.7	843
CS01	26.6	1.7	17.6	240	7.4	204	11.8	70	67	22.1	N/A	72	1176	29	126	14	7.1	776
K6-68	N/A		26.2	231	34.7	30.8	24.7	96	100	N/A	N/A	97	989	30	267	16	N/A	816
STJ02	10.2	0.3	4.8	55	6.6	6.9	5.6	61	80	22.3	N/A	110	885	20	19	18	2.3	751
QTY03	9.0	2.0	4.6	50	7.6	5.3	4.3	67	73	21.7	N/A	118	1098	11	64	13	1.2	948
MJ01	37.2	2.5	9.8	137	8.3	15	5.8	27	85	21.6	N/A	87	665	21	102	15	4.5	824
DLC01	7.1	1.7	7.8	82	13.6	13.8	5.7	27	37	20.6	N/A	79	921	12	30	12	1.4	1048
MLT02	16.4	1.9	11.4	184	6.9	17.9	3.7	40	108	22.8	N/A	91	1181	31	94	14	3.0	787
JC-019	6.4	2.1	7.5	86	6.3	6.4	6.9	32	38	18.4	1.1	95	1117	14	146	11	N/A	1014
JC-018	5.9	2.2	7.6	94	6.5	6.4	8.2	18	40.7	19.3	N/A	72	1173	15	169	12	N/A	983
SK3402	17.7	2.0	9.1	99	8.2	10.3	9.4	17	51.7	21.2	1.1	70	966	16	156	12	N/A	915
JC-012	10	1.9	9.9	109	11.4	7.0	10.8	40	34.5	19.5	5.7	59	1960	15	147	9	N/A	1284
JY-2h	35.4	2.1	12.6	152	1.9	16.3	9.87	41	141	26.6	2.0	65	1060	26	261	20	2.7	921
JY-3h	32.1	2.1	11.8	148	2.2	16.3	10.9	42	136	25.2	2.2	56	1020	25	235	19	2.5	874
JY-4h	57.6	0.9	36.9	413	6.4	48.3	31	53	275	22.7	14.5	70	590	29	118	8	4.7	320
JY-5h	31.5	2.2	12.3	161	3.1	17.7	11	51	158	25.5	4.2	64	1190	28	243	21	3.9	940
JY-6h	31.7	2.0	11.2	134	2.0	15.7	9.78	201	141	25.2	6.3	71	1280	26	218	19	3.0	936
JY-2	41.2	0.9	33.2	453	3.3	57.3	34.1	239	190	22.5	18.5	54	370	25	136	8	3.9	176
JY-3	32.5	0.7	30.7	679	6.2	54	30.8	87	361	28.4	11.9	63	499	22	95	8	4.6	276
JY-4	16.6	1.5	11.5	100	1.1	19.5	12.1	528	88.2	24	7.7	10	1310	24	175	19	1.2	566
JY-5	14.2	0.8	30.4	516	3.3	62.7	47.4	199	180	23.3	11.4	25	440	30	73	6	1.6	219
JY-6	47.4	0.8	28.8	385	7.1	42.6	28.5	77	248	21.1	10.6	54	642	29	108	9	3.5	294

Table S-1 continued

Samples	La	Ce	Pr	Nd	Sm	Eu	Gd	Tb	Dy	Ho	Er	Tm	Yb	Lu	Hf	Ta	Pb	Th	U
XTJ-14	37.6	69	8.1	30	5.3	1.5	4.5	0.7	3.7	0.7	2	0.3	2	0.3	1.1	1.1	8.1	10.2	2.9
CS01	51.7	103	12.6	49	9.1	2.5	7.7	1.2	6.0	1.0	3.0	0.5	2.6	0.4	4.5	1.1	12.8	9.1	2.1
K6-68*	70.5	142	15.6	60	13.8	3.4	11.1	1.4	7.0	1.2	3.1	0.39	2.49	0.4	7.0	0.9	16.2	12.2	2.8
STJ02	32.2	52	5.1	19	4.3	1.1	2.7	0.5	1.6	0.4	1.2	0.2	0.9	0.2	4.4	0.9	6.8	8.5	3.4
QTY03	34.1	65	7.5	27	4.7	1.2	3.7	0.5	2.2	0.4	1.0	0.2	0.9	0.1	2.4	0.9	15.8	7.2	2.3
MJ01	49.2	90	10.2	38	6.6	1.8	5.6	0.8	4.1	0.8	2.2	0.3	2.0	0.3	3.6	1.1	10.7	11.2	3.1
DLC01	24.5	44	5.8	23	4.6	1.5	3.8	0.5	2.4	0.4	1.0	0.2	0.9	0.1	1.3	0.8	5.9	3.7	1.2
MLT02	48.2	96	11.9	47	8.5	2.5	7.5	1.1	5.9	1.1	3.2	0.5	2.9	0.5	3.7	0.9	11.7	8.5	2.2
JC-019*	32.7	60	7.0	27	4.7	1.4	3.9	0.6	2.9	0.6	1.6	0.2	1.4	0.2	4.7	0.8	9.9	7.7	2.4
JC-018*	42.8	76	8.7	32	5.4	1.7	4.4	0.6	3.4	0.6	1.9	0.3	1.7	0.3	5.3	0.9	10.1	9.4	3.1
SK3402*	39.7	74	8.2	32	5.4	1.7	4.2	0.7	3.4	0.6	1.8	0.3	1.7	0.3	4.8	0.8	7.6	7.9	2.6
JC-012*	37.0	65	7.7	30	5.2	1.5	4.0	0.6	3.3	0.6	1.7	0.3	1.6	0.3	4.6	0.7	5.6	7.8	2.7
JY-2h	50.0	97	11.5	49	9.2	2.4	7.0	1.0	5.1	0.9	2.7	0.4	2.5	0.4	5.7	1.1	23.5	12.2	3.0
JY-3h	47.6	78	11.5	43	8.4	2.5	6.5	1.0	5.0	0.8	2.6	0.4	2.3	0.4	5.1	1.2	19.1	10.6	2.6
JY-4h	33.9	69	11.7	46	12.0	3.2	9.3	1.3	6.4	1.1	2.6	0.3	2.1	0.3	3.9	0.5	14.2	4.6	1.2
JY-5h	53.0	96	12.0	50	9.4	2.5	6.8	1.0	5.1	0.9	2.6	0.4	2.4	0.4	5.7	1.1	20.5	12.3	3.1
JY-6h	53.1	94	12.6	43	8.6	2.6	6.1	1.0	4.9	0.8	2.5	0.3	2.3	0.3	5.4	1.0	20.8	12.2	2.7
JY-2*	36.5	77	10.6	46	10.8	2.8	8.9	1.2	5.9	1.0	2.4	0.3	1.9	0.3	4.1	0.5	23.8	5.8	2.4
JY-3	28.3	62	8.6	37	8.4	2.3	7.1	1.0	5.1	0.8	2.0	0.3	1.7	0.2	3.0	0.5	13.2	3.5	1.3
JY-4	38.9	65	9.7	37	6.8	1.8	5.2	0.8	4.3	0.7	2.2	0.3	2.2	0.3	4.2	1.1	16.4	7.5	2.2
JY-5	41.1	85	11.9	52	12.5	3.4	8.4	1.3	6.6	1.0	2.7	0.3	1.9	0.3	2.8	0.4	6.5	2.3	1.3
JY-6	32.7	72	10.3	47	11.4	2.9	8.1	1.3	6.6	1.0	2.7	0.3	2.1	0.3	3.2	0.5	10.1	3.4	1.0

*data are collected from Du *et al.*(2016), Du and Audétat (2020); N/A :not available

Table S-2 Major elements of amphibole and clinopyroxene in cumulates (all values in wt.%).

Samples	Minerals	SiO_2	TiO_2	Al_2O_3	Cr_2O_3	FeOT	MnO	MgO	CaO	Na_2O	K_2O	P_2O_5	Total	P/kbar	T/°C	fO_2/ (ΔFMQ)
JY2*	amph	41.4	3.0	13.9	N/A	12.5	0.1	12.9	12.3	2.5	1.0	N/A	99.8	N/A	985	1.1
JY2*	amph	41.4	3.0	13.8	N/A	12.1	0.1	13.1	12.4	2.9	1.0	N/A	100	N/A	1001	1.1
JY2*	amph	41.4	3.1	13.9	N/A	12.4	0.1	12.6	12.4	2.9	1.1	N/A	99.9	N/A	997	0.9
JY2*	amph	40.9	3.1	14.2	N/A	12.6	0.1	12.8	12.3	2.9	0.9	N/A	99.9	N/A	1007	0.9
JY2*	amph	41.5	3.4	13.3	N/A	12.4	0.2	12.8	12.2	2.8	1.0	N/A	99.9	N/A	997	0.9
JY2*	cpx	49.2	1.1	4.1	N/A	8.8	0.3	13.8	21.8	0.5	N/A	N/A	99.6	6.6	1083	1.1
JY2*	cpx	48.4	1.0	4.2	N/A	8.7	0.3	13.9	21.9	0.5	N/A	N/A	98.9	5.6	1082	0.8
JY2*	cpx	49.3	1.0	3.8	N/A	9.3	0.3	13.6	21.2	0.5	N/A	0.1	99.2	5.4	1075	0.9
JY2*	cpx	49.4	0.9	3.2	N/A	9.3	0.3	13.9	21.1	0.5	N/A	0.1	98.7	5.8	1079	0.8
JY3	amph	38.7	3.1	14.1	0.1	10.7	0.1	14.0	11.9	2.1	1.8	N/A	96.6	5.0	1016	0.9
JY3	amph	39.4	2.9	13.9	N/A	10.9	N/A	13.7	11.8	2.1	2.0	N/A	96.8	4.8	1001	1.3
JY3	amph	39.1	2.9	13.9	N/A	11.6	0.1	13.4	12.1	2.1	1.8	0.1	97.2	4.8	1002	0.9
JY3	cpx	48.9	1.1	3.9	N/A	9.2	0.4	13.7	21.7	0.5	N/A	N/A	99.4	3.8	1032	N/A
JY3	cpx	48.9	1.2	4.2	N/A	9.1	0.3	13.7	21.6	0.5	N/A	0.1	99.6	5.1	1044	N/A
JY3	cpx	48.7	1.1	4.7	N/A	8.6	0.3	13.6	21.9	0.5	N/A	0.1	99.4	6.0	1049	N/A
JY4	amph	39.1	3.1	13.9	N/A	11.3	0.2	13.7	12.2	2.0	1.9	N/A	97.5	4.7	1006	1
JY4	amph	40.1	3.1	13.4	N/A	11.2	0.1	13.3	12	2.1	1.8	0.1	97.3	4.2	990	1.1
JY4	amph	40.4	3.0	13.2	0.3	11.8	0.1	12.3	11.9	2.4	2.0	0.1	97.7	N/A	988	N/A
JY4	amph	39.7	3.0	13.2	N/A	11.5	0.1	14.0	11.5	2.3	1.9	N/A	97.2	4.1	1001	1.2
JY4	cpx	49.0	1.2	4.2	N/A	8.5	0.2	13.6	22	0.5	N/A	0.1	99.4	6.2	1049	N/A
JY4	cpx	48.5	1.1	4.5	N/A	8.8	0.3	14.1	22	0.5	N/A	0.0	99.9	4.5	1039	N/A
JY4	cpx	48.1	1.2	5.0	N/A	8.5	0.2	13.5	22.4	0.5	N/A	0.1	99.6	5.6	1043	N/A
JY4	cpx	48.2	1.1	4.4	N/A	8.9	0.3	13.8	22.2	0.4	N/A	N/A	99.2	3.3	1026	N/A
JY5	amph	39.1	3.1	13.7	N/A	11.7	0.1	13.1	12.1	2.4	1.9	0.1	97.3	4.6	1010	0.7
JY5	amph	38.4	3.1	14.8	0.3	12.6	0.1	11.5	11.7	2.8	2.1	0.1	97.5	5.7	1024	N/A
JY5	amph	39.8	2.8	13.6	N/A	12.0	0.2	13	12	2.4	1.8	0.2	97.9	4.4	994	0.8
JY5	cpx	48.8	0.9	4.2	N/A	8.4	0.3	14.3	21.6	0.4	N/A	N/A	99.1	5.2	1046	N/A
JY5	cpx	48.8	0.9	4.2	0.0	8.4	0.3	14.3	21.6	0.4	0.0	0.0	99.4	4.9	1040	N/A
JY5	cpx	49.1	1.1	4.0	0.0	8.6	0.2	14.0	22.0	0.4	0.0	0.0	98.9	N/A	1009	N/A
JY5	cpx	48.8	1.0	3.7	0.0	8.5	0.2	14.2	22.0	0.4	0.0	0.0	99.8	4.3	1046	N/A
JY6	cpx	48.5	1.1	4.3	0.0	9.4	0.4	13.7	21.8	0.6	0.0	0.0	98.8	N/A	1030	N/A
JY6	cpx	49.1	1.1	4.0	0.0	9.0	0.3	14.1	21.5	0.5	0.0	0.1	99.8	5.2	1056	N/A
JY6	cpx	48.0	1.1	4.4	0.0	9.5	0.3	13.5	21.3	0.6	0.0	0.1	99.0	5.8	1062	N/A
JY6	cpx	49.5	0.9	4.6	0.0	9.1	0.2	12.2	20.3	0.6	1.1	0.2	98.8	7.0	1055	N/A
JY6	amph	39.1	3.2	13.1	0.0	12.9	0.2	12.4	11.5	2.1	2.0	0.1	96.6	4.1	982.2	0.7
JY6	amph	40.4	3.0	12.2	0.1	13.1	0.2	13.0	11.6	2.3	1.8	0.0	97.7	3.2	968.6	1.1
JY6	amph	40.6	2.8	12.1	0.0	13.1	0.2	13.0	11.6	2.3	1.8	0.1	97.6	3.1	963.6	1.0
JY6	amph	40.2	3.1	12.4	0.1	12.7	0.3	13.1	11.7	2.2	1.7	0.0	97.5	3.4	973.7	1.0

N/A:not available

Table S-3 Mass balance calculations of amphibole-dominated Fractional Crystallization.

Inputted parameters	Compositions	SiO_2	TiO_2	Al_2O_3	FeOt	MnO	MgO	CaO	Na_2O	K_2O	P_2O_5
Parent magma	SMIs in cumulate	49.13	1.68	14.78	9.09	0.16	8.11	10.19	3.28	2.79	0.78
Fractionated minerals	amph (92.5 vol %)	40.89	3.11	13.79	12.31	0.15	13.31	12.21	2.45	1.68	0.09
	cpx (7.5 vol %)	49.11	1.06	4.22	8.93	0.29	13.85	21.82	0.49	0.16	0.07
Daughter magma	calculated melt	59.31	0.21	17.15	5.74	0.16	2.04	7.14	4.52	4.32	1.62
	actual melt	59.49	0.87	17.29	4.96	0.12	2.41	6.78	4.37	3.33	0.38
R^2	**0.998675**										

Using the average composition of silicate melt inclusions (SMIs) from cumulate rocks in the Tongling area as the initial magma (Du and Audétat, 2020), and the compositions of actual amphibole and clinopyroxene from these cumulates as fractionating phases, the modal simulated the crystallization of a mineral assemblage consisting of 92.5 vol. % amphibole and 7.5 vol. % clinopyroxene. The results demonstrate that after approximately 53 % fractional crystallization, the calculated composition of the residual melt shows an excellent match with the average composition of the actual natural magmas. This remarkably high degree of consistency is quantitatively confirmed by an R^2 value of 0.998675, indicating that amphibole-dominated fractionation is a highly viable process for generating the evolved magmas observed in the Tongling region.

amph–amphibole; cpx–clinopyroxene

Table S-4 Trace elements of amphibole, clinopyroxene and magnetite in cumulates (all values in ppm).

Sample	mineral	Na	Mg	Al	Si	P	Sc	Ti	V	Cr	Mn	Fe	Co
JY2	mgt	7	460	6350	2132	16	2	8681	2257	28	1330	726720	62
JY2	mgt	33	435	5976	2040	13	2	11791	2255	30	1621	723006	64
JY2	mgt	21	548	6889	1343	38	2	8201	2247	28	1346	727464	70
JY2	mgt	6	448	6342	1736	2	2	6961	2402	22	1169	729177	62
JY2	mgt	5	994	10333	1978	41	2	7814	2137	17	1444	721517	99
JY2	mgt	24	1007	10631	1783	54	2	11576	2146	24	1778	715963	101
JY3	mgt	13	1061	10297	1696	24	2	12318	2057	25	1976	715505	99
JY3	mgt	7	1275	10171	1512	47	3	16098	2106	24	2724	710451	97
JY3	mgt	0	688	8529	1426	45	1	6202	2134	22	1101	727305	85
JY4	mgt	7	746	8278	1765	29	1	6207	2163	23	1107	727182	88
JY4	mgt	6	563	6887	1390	50	1	8555	2198	24	1273	727206	58
JY4	mgt	7	555	6839	1843	38	1	7614	2128	24	1196	727930	61
JY5	mgt	7	802	8477	1645	37	2	15278	2059	21	2097	714652	67
JY5	mgt	38	639	7733	1733	50	1	7590	2096	22	1144	726624	55
JY5	mgt	2	516	6740	1693	41	1	6302	2255	19	1104	729674	35
JY5	mgt	34	723	8330	1822	30	2	8166	2265	5	1371	724269	64
JY5	mgt	8	471	6474	1628	43	1	5882	2256	26	1055	730760	37
JY6	mgt	2	1268	9384	1902	20	2	11969	2116	34	2245	716246	125
JY6	mgt	27	1018	3881	7576	27	2	9753	2263	30	1452	713655	93

Table S-4 continued

Sample	mineral	Ni	Cu	Zn	Ga	Ge	As	Zr	Mo
JY2	mgt	73	0.11	745	58	0.6	1.9	1.4	1.7
JY2	mgt	75	0.68	991	55	0.3	2.1	1.3	1.3
JY2	mgt	75	0.37	1123	55	0.8	1.5	1.5	1.0
JY2	mgt	72	0.00	1245	51	0.4	2.4	2.0	3.0
JY2	mgt	93	0.08	1034	60	0.4	0.0	1.8	1.2
JY2	mgt	89	1.15	1363	59	0.3	2.5	2.0	1.5
JY3	mgt	91	1.74	1433	58	0.3	0.0	2.4	1.4
JY3	mgt	86	1.00	1078	55	0.5	0.8	2.3	1.6
JY3	mgt	82	0.33	1514	52	0.5	0.2	1.5	1.3
JY4	mgt	89	0.57	1383	47	0.3	0.0	1.9	1.7
JY4	mgt	61	0.00	1003	52	0.4	1.2	2.0	1.2
JY4	mgt	63	0.12	938	52	0.7	3.1	1.7	1.8
JY5	mgt	64	0.27	1474	54	0.8	0.6	1.9	1.2
JY5	mgt	70	0.49	1087	49	0.5	2.1	1.5	1.6
JY5	mgt	83	0.49	1298	45	0.1	1.9	1.6	1.5
JY5	mgt	86	0.61	1132	52	0.2	0.9	1.0	1.1
JY5	mgt	80	0.89	1301	46	0.7	2.1	2.1	2.1
JY6	mgt	89	0.35	1160	55	0.4	2.4	2.1	2.5
JY6	mgt	95	1.25	1040	36	0.6	0.2	2.7	2.0

Table S-4 continued

Sample	mineral	Li	B	Sc	V	Cr	Co	Ni	Cu	Zn	Ga	Rb	Sr	Y
JY2	cpx	16	N/A	53	182	104	23	28	0.8	31	N/A	3	84	15
JY2	cpx	21	N/A	56	198	112	29	27	7.1	35	N/A	3	88	20
JY2	cpx	25	N/A	60	205	38	35	25	6.9	34	N/A	1	105	22
JY3	cpx	23	N/A	70	214	27	37	31	1.4	46	N/A	1	111	26
JY3	cpx	29	N/A	68	206	20	33	29	1.8	55	N/A	3	204	28
JY3	cpx	52	17	56	156	11	28	14	1.3	69	7	2	178	34
JY3	cpx	76	16	54	140	7	29	10	1.4	85	6	0	71	41
JY4	cpx	18	N/A	55	190	108	26	27	3.9	33	N/A	3	86	18
JY4	cpx	23	N/A	58	202	75	32	26	7.0	35	N/A	2	97	21
JY4	cpx	24	N/A	65	209	33	36	28	4.2	40	N/A	1	108	24
JY4	cpx	26	N/A	69	210	24	35	30	1.6	50	N/A	2	157	27
JY5	cpx	41	N/A	62	181	15	31	21	1.5	62	7	3	191	31
JY5	cpx	64	17	55	148	9	29	12	1.3	77	6	1	124	37
JY5	cpx	47	N/A	54	165	58	27	19	2.7	59	6	2	78	29
JY5	cpx	20	N/A	56	196	92	29	27	5.5	34	N/A	2	92	20
JY6	cpx	23	N/A	62	206	54	34	27	5.6	37	N/A	1	103	23
JY6	cpx	25	N/A	67	210	28	35	29	2.9	45	N/A	2	133	26
JY2	amph	2	13	50	461	14	52	11	2.5	108	17	4	548	23
JY2	amph	2	12	51	451	16	53	11	1.2	107	16	4	531	23
JY2	amph	2	11	50	436	15	54	13	0.8	109	16	4	442	21
JY3	amph	3	12	50	436	16	54	14	1.0	109	16	4	451	21
JY3	amph	3	12	50	450	16	53	12	1.6	110	16	4	516	23
JY3	amph	3	11	52	447	54	56	50	1.4	114	17	8	604	24
JY3	amph	2	12	50	456	15	53	11	1.8	107	17	4	539	23
JY4	amph	2	12	50	443	16	54	12	1.0	108	16	4	486	22
JY4	amph	3	12	50	436	16	54	14	0.9	109	16	4	446	21
JY4	amph	3	12	50	443	16	54	13	1.3	110	16	4	483	22
JY4	amph	3	12	51	449	35	54	31	1.5	112	16	6	560	23
JY5	amph	3	12	51	451	35	54	31	1.6	111	17	6	572	23
JY5	amph	2	12	50	450	15	53	12	1.4	108	16	4	513	22
JY5	amph	2	12	50	440	16	54	13	1.0	108	16	4	466	22
JY5	amph	3	12	50	440	16	54	13	1.1	109	16	4	465	22
JY6	amph	3	12	50	446	26	54	22	1.4	111	16	5	522	23
JY6	amph	3	12	51	450	35	54	31	1.5	111	17	6	566	23

Table S-4 continued

Sample	Mineral	Zr	Nb	Sn	Ba	La	Ce	Pr	Nd	Sm	Eu	Gd	Tb
JY2	cpx	89	0.2	N/A	42	10.7	31.6	4.9	26.2	6.6	2.1	6.3	0.8
JY2	cpx	87	0.2	N/A	27	11.4	35.5	5.7	30.2	8.5	2.5	7.7	1.0
JY2	cpx	58	0.1	N/A	7	7.1	28.2	5.2	30.5	9.2	2.5	8.2	1.0
JY3	cpx	73	0.1	N/A	3	10.0	37.3	6.5	36.8	10.8	2.9	10.1	1.2
JY3	cpx	114	0.3	N/A	12	14.2	48.3	7.8	41.7	11.9	3.3	10.6	1.3
JY3	cpx	98	0.3	2	11	14.9	47.6	7.3	39.1	10.7	2.8	9.4	1.3
JY3	cpx	68	0.1	2	1	14.9	46.8	7.2	39.4	10.1	2.4	9.8	1.4
JY4	cpx	88	0.2	N/A	35	11.0	33.5	5.3	28.2	7.6	2.3	7.0	0.9
JY4	cpx	72	0.2	N/A	17	9.3	31.9	5.4	30.4	8.8	2.5	7.9	1.0
JY4	cpx	65	0.1	N/A	5	8.6	32.8	5.8	33.7	10.0	2.7	9.1	1.1
JY4	cpx	93	0.2	N/A	7	12.1	42.8	7.2	39.2	11.4	3.1	10.4	1.3
JY5	cpx	106	0.3	2	11	14.6	48.0	7.6	40.4	11.3	3.0	10.0	1.3
JY5	cpx	83	0.2	2	6	14.9	47.2	7.3	39.3	10.4	2.6	9.6	1.4
JY5	cpx	78	0.2	2	18	13.0	40.1	6.2	33.8	8.8	2.4	8.4	1.1
JY5	cpx	80	0.2	N/A	26	10.2	32.7	5.4	29.3	8.2	2.4	7.4	0.9
JY6	cpx	69	0.1	N/A	11	8.9	32.3	5.6	32.0	9.4	2.6	8.5	1.1
JY6	cpx	79	0.2	N/A	6	10.4	37.8	6.5	36.5	10.7	2.9	9.7	1.2
JY2	amph	52	5.4	3	274	7.2	25.7	4.2	23.6	6.5	1.9	6.1	0.8
JY2	amph	49	5.3	3	253	6.9	25.1	4.2	24.0	6.3	1.9	6.4	0.9
JY2	amph	52	4.7	3	217	6.9	25.2	4.1	23.4	6.0	1.8	5.7	0.8
JY3	amph	51	4.6	3	223	7.0	25.5	4.2	23.5	6.3	1.8	5.7	0.8
JY3	amph	50	5.2	3	251	7.0	25.3	4.2	24.0	6.7	1.9	6.5	0.9
JY3	amph	67	5.9	3	294	10.9	38.7	6.5	37.0	9.6	3.0	9.0	1.1
JY3	amph	50	5.3	3	264	7.0	25.4	4.2	23.8	6.4	1.9	6.2	0.8
JY4	amph	51	5.0	3	235	6.9	25.1	4.1	23.7	6.2	1.9	6.1	0.8
JY4	amph	52	4.6	3	220	7.0	25.3	4.2	23.4	6.2	1.8	5.7	0.8
JY4	amph	51	4.9	3	237	7.0	25.4	4.2	23.7	6.5	1.9	6.1	0.8
JY4	amph	58	5.5	3	273	8.9	32.0	5.4	30.5	8.1	2.4	7.8	1.0
JY5	amph	59	5.6	3	279	9.0	32.0	5.4	30.4	8.0	2.5	7.6	1.0
JY5	amph	51	5.2	3	249	7.0	25.2	4.2	23.7	6.3	1.9	6.1	0.8
JY5	amph	51	4.8	3	227	6.9	25.2	4.2	23.6	6.2	1.8	5.9	0.8
JY5	amph	51	4.8	3	228	7.0	25.4	4.2	23.6	6.4	1.8	5.9	0.8
JY6	amph	55	5.2	3	255	8.0	28.7	4.8	27.1	7.3	2.1	6.9	0.9
JY6	amph	58	5.6	3	276	9.0	32.0	5.4	30.5	8.1	2.4	7.7	1.0

Table S-4 continued

Sample	Mineral	Dy	Ho	Er	Tm	Yb	Lu	Hf
JY2	cpx	3.7	0.6	1.4	0.1	1.0	0.1	2.9
JY2	cpx	4.9	0.8	1.9	0.2	1.5	0.2	3.4
JY2	cpx	5.5	0.9	2.1	0.3	1.6	0.2	2.9
JY3	cpx	6.0	1.0	2.4	0.3	1.9	0.3	2.9
JY3	cpx	6.4	1.1	2.5	0.3	2.4	0.3	4.4
JY3	cpx	7.1	1.3	3.2	0.4	2.9	0.4	3.7
JY3	cpx	8.1	1.5	4.1	0.5	3.5	0.5	2.4
JY4	cpx	4.3	0.7	1.6	0.2	1.3	0.2	3.2
JY4	cpx	5.2	0.8	2.0	0.2	1.6	0.2	3.1
JY4	cpx	5.8	1.0	2.3	0.3	1.8	0.2	2.9
JY4	cpx	6.2	1.1	2.5	0.3	2.1	0.3	3.7
JY5	cpx	6.7	1.2	2.9	0.4	2.6	0.3	4.0
JY5	cpx	7.6	1.4	3.6	0.5	3.2	0.5	3.0
JY5	cpx	6.2	1.1	2.8	0.4	2.4	0.3	2.8
JY5	cpx	4.7	0.8	1.8	0.2	1.4	0.2	3.2
JY6	cpx	5.5	0.9	2.1	0.3	1.7	0.2	3.0
JY6	cpx	6.0	1.0	2.4	0.3	1.9	0.3	3.3
JY2	amph	4.7	0.9	2.1	0.3	1.6	0.2	1.8
JY2	amph	4.8	0.9	2.1	0.3	1.5	0.2	1.7
JY2	amph	4.6	0.8	1.9	0.3	1.5	0.2	1.9
JY3	amph	4.7	0.8	1.9	0.3	1.6	0.2	1.9
JY3	amph	4.9	0.9	2.0	0.3	1.6	0.2	1.7
JY3	amph	5.5	0.9	2.1	0.2	1.5	0.2	2.6
JY3	amph	4.7	0.9	2.1	0.3	1.5	0.2	1.7
JY4	amph	4.7	0.9	2.0	0.3	1.5	0.2	1.8
JY4	amph	4.6	0.8	1.9	0.3	1.5	0.2	1.9
JY4	amph	4.8	0.9	2.0	0.3	1.6	0.2	1.8
JY4	amph	5.2	0.9	2.1	0.3	1.6	0.2	2.2
JY5	amph	5.1	0.9	2.1	0.3	1.5	0.2	2.2
JY5	amph	4.7	0.9	2.1	0.3	1.5	0.2	1.8
JY5	amph	4.7	0.8	2.0	0.3	1.5	0.2	1.8
JY5	amph	4.7	0.8	1.9	0.3	1.6	0.2	1.9
JY6	amph	5.0	0.9	2.0	0.3	1.6	0.2	2.0
JY6	amph	5.1	0.9	2.1	0.3	1.5	0.2	2.2

Supplementary Figures

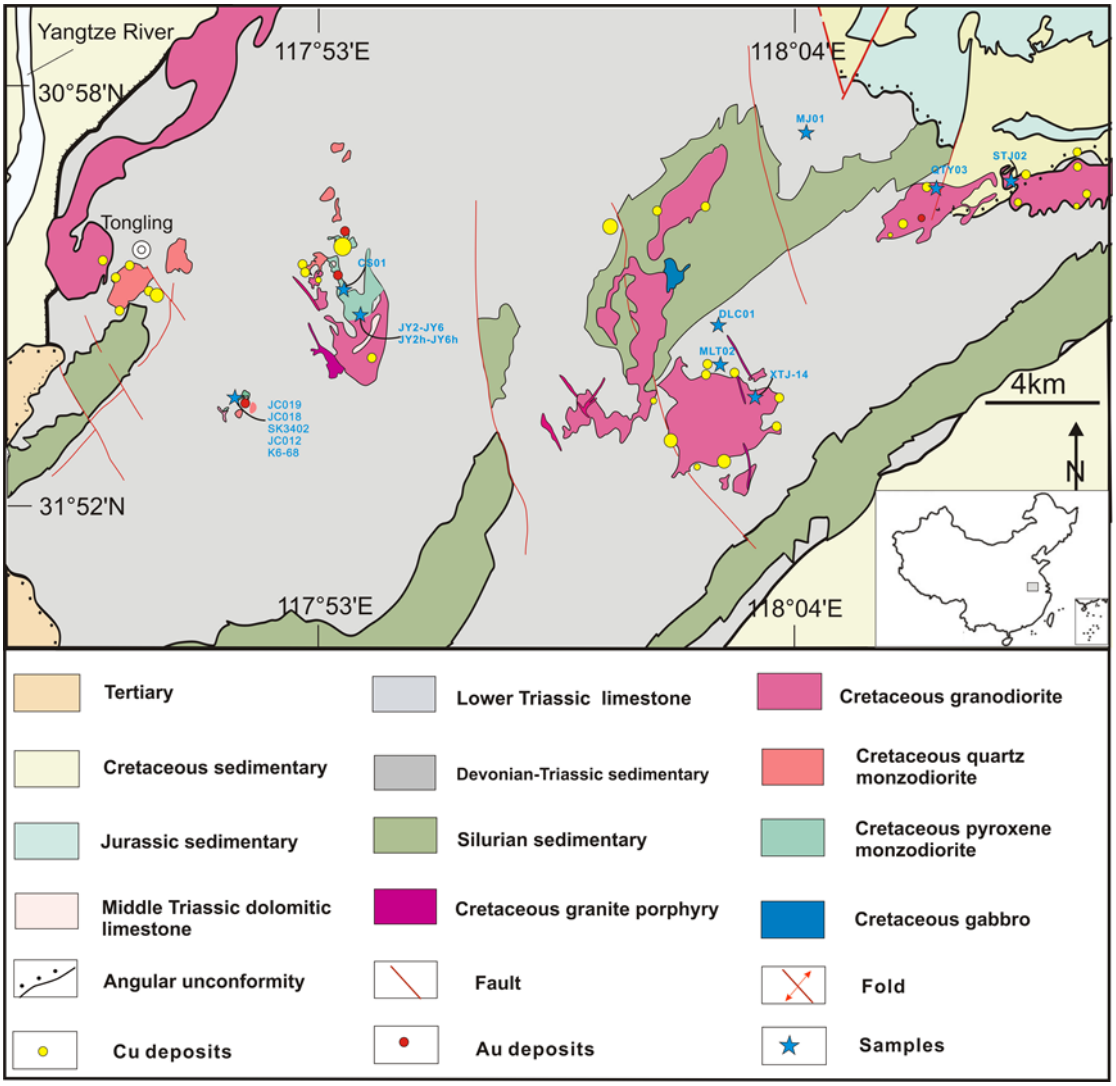

Figure S-1 Geological map of Tongling ore district with sample locations.

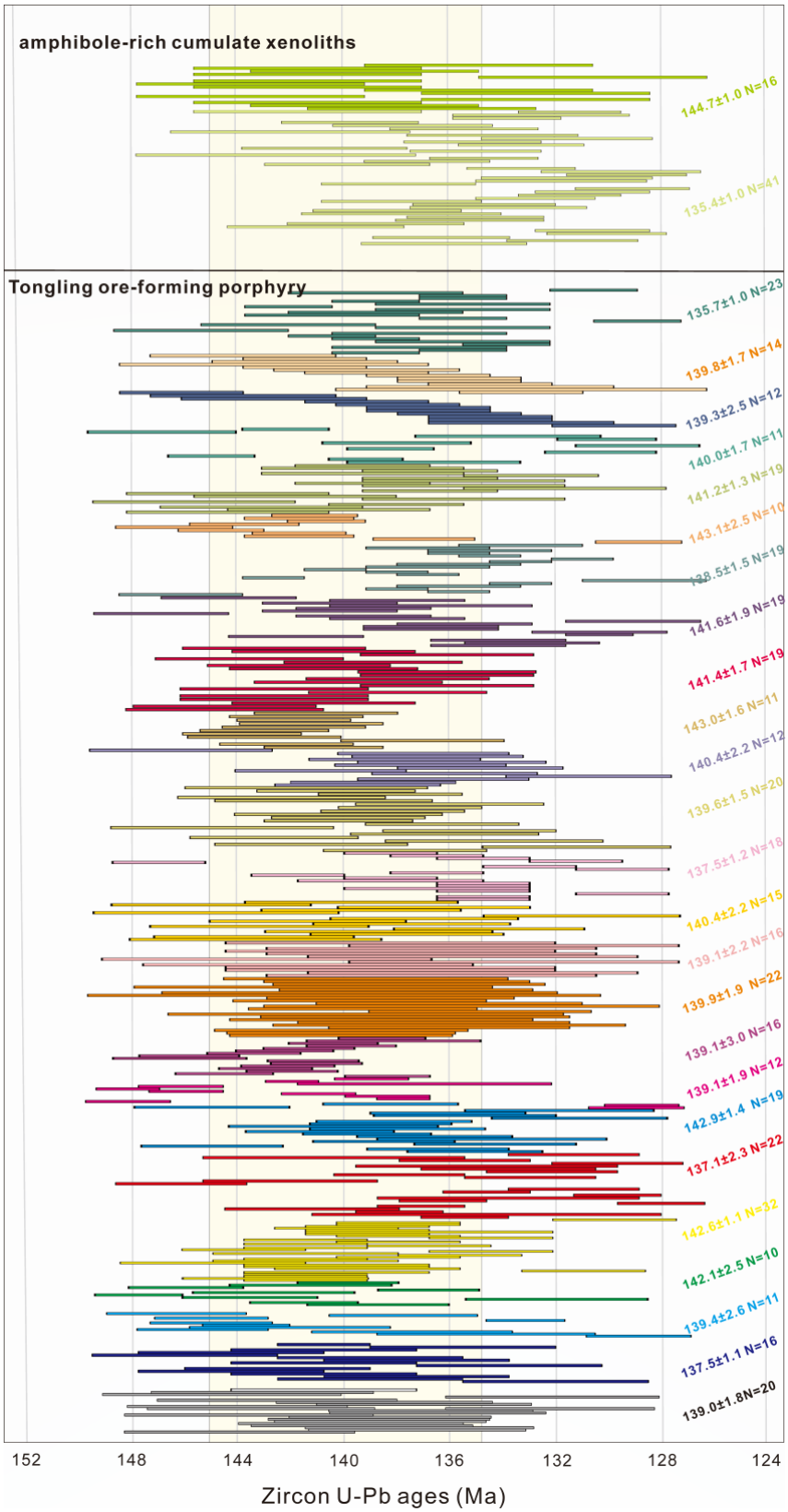

Figure S-2 Zircon U-Pb ages of ore-forming porphyries and cumulates xenoliths. The picture is modified from the supplementary material of Du *et al.* (2025). Age data of ore-forming porphyries and amphibole-rich cumulates are from Xie *et al.* (2008, 2009), Wu *et al.* (2010), Yang *et al.* (2011), Lai *et al.* (2012), Li *et al.* (2014), Wang *et al.* (2016), Du *et al.* (2016) and Hu *et al.* (2018).

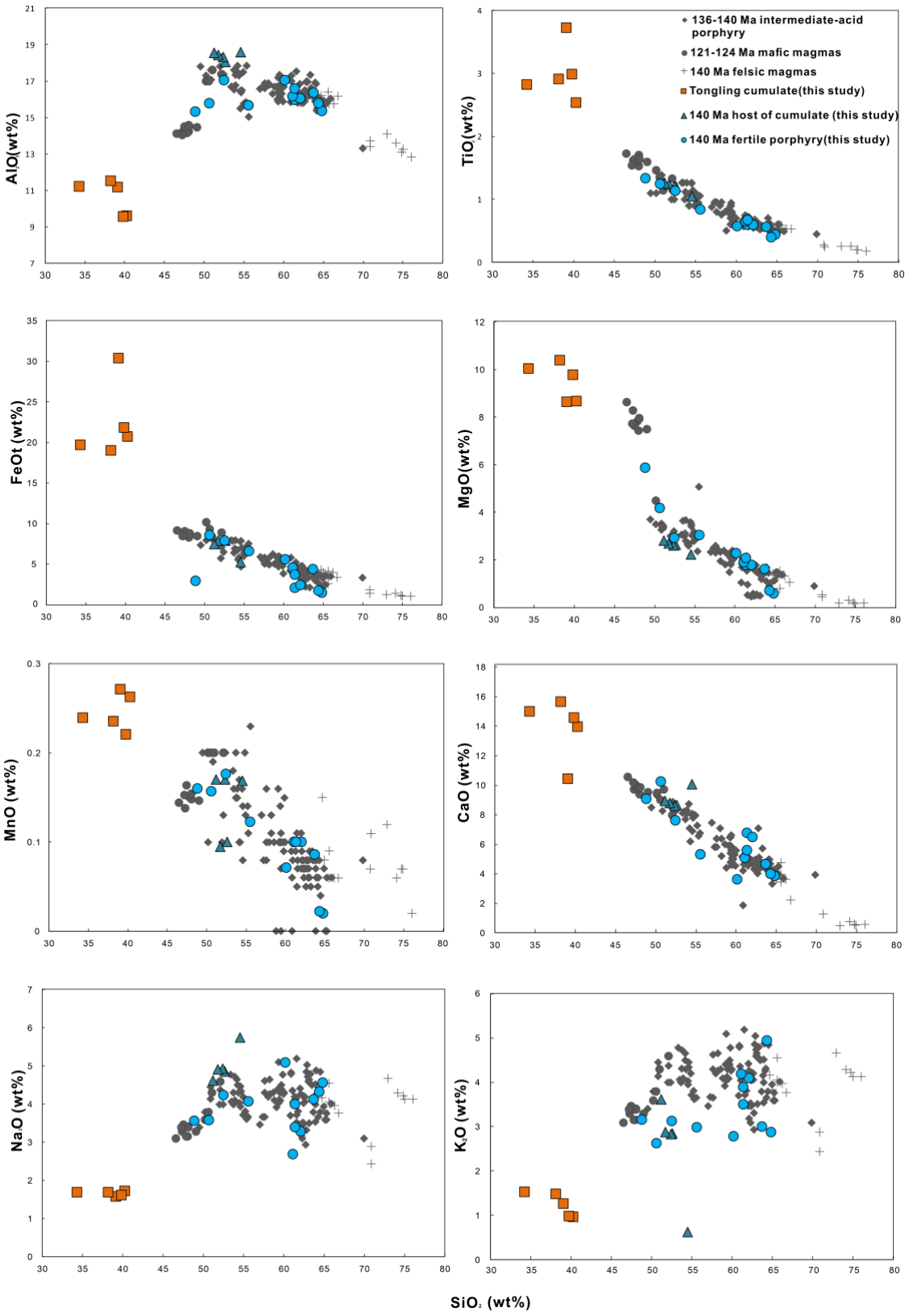

Figure S-3 Hark diagram of ore-forming magmas (136-145 Ma), amphibole-rich cumulates, and 121-124 Ma mafic magmas. The Tongling whole-rock data are from Wang *et al.* (2003), Wang *et al.* (2015, 2016), Huang *et al. (*2004), Yan *et al.* (2008), Xie *et al.* (2012a, b), Guo *et al.* (2013), Li *et al.* (2014), Chen *et al.* (2016), and Du *et al.*(2018).

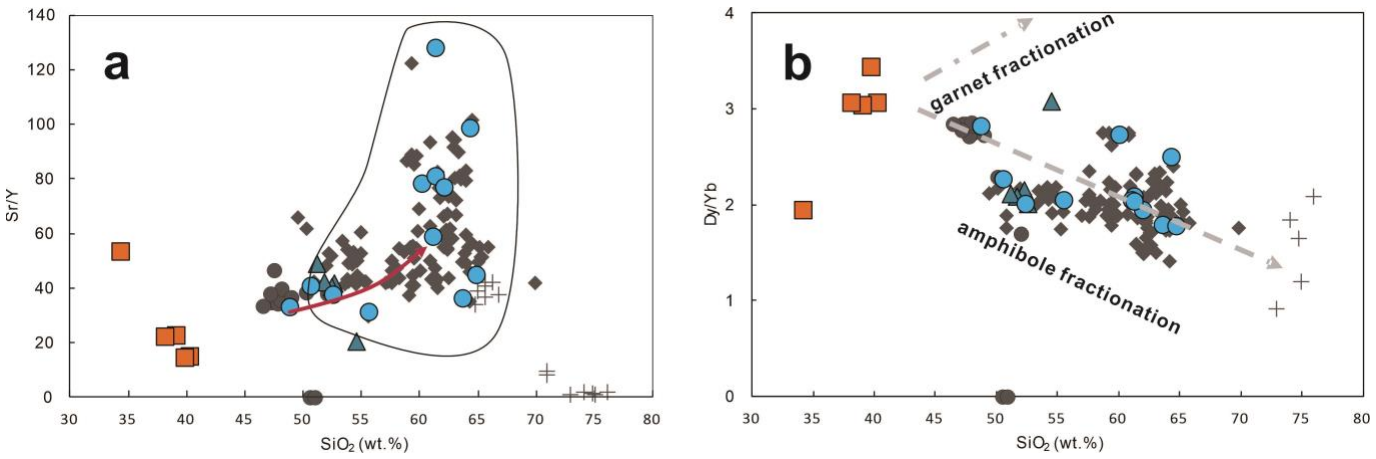

Figure S-4 Trace element signature of cumulate, mafic magmas (121-124 Ma) and ore-forming magmas (136-145 Ma). **(a)** fields of barren *vs*. porphyry Cu±Au±Mo productive magmas are from Loucks (2014); the arrow shows the predicted fractionation trend for crystallization of 50 wt. % amphibole ($D_{Sr}^{amph/melt}$ = 0.60; $D_{Y}^{amph/melt}$ = 1.2; $D_{SiO2}^{amph/melt}$ =0.80), 40 wt. % clinopyroxene ($D_{Sr}^{cpx/melt}$ = 0.13; $D_{Y}^{cpx/melt}$ = 0.80; D_{SiO2} cpx/melt =1.0) and 10 wt. % magnetite ($D_{Sr}^{mgt/melt}$ = 0; $D_{Y}^{mgt/melt}$ = 0; $D_{SiO2}^{mgt/melt}$ = 0); **(b)** Garnet *versus* amphibole fractionation trends are from Davidson *et al.* (2007).

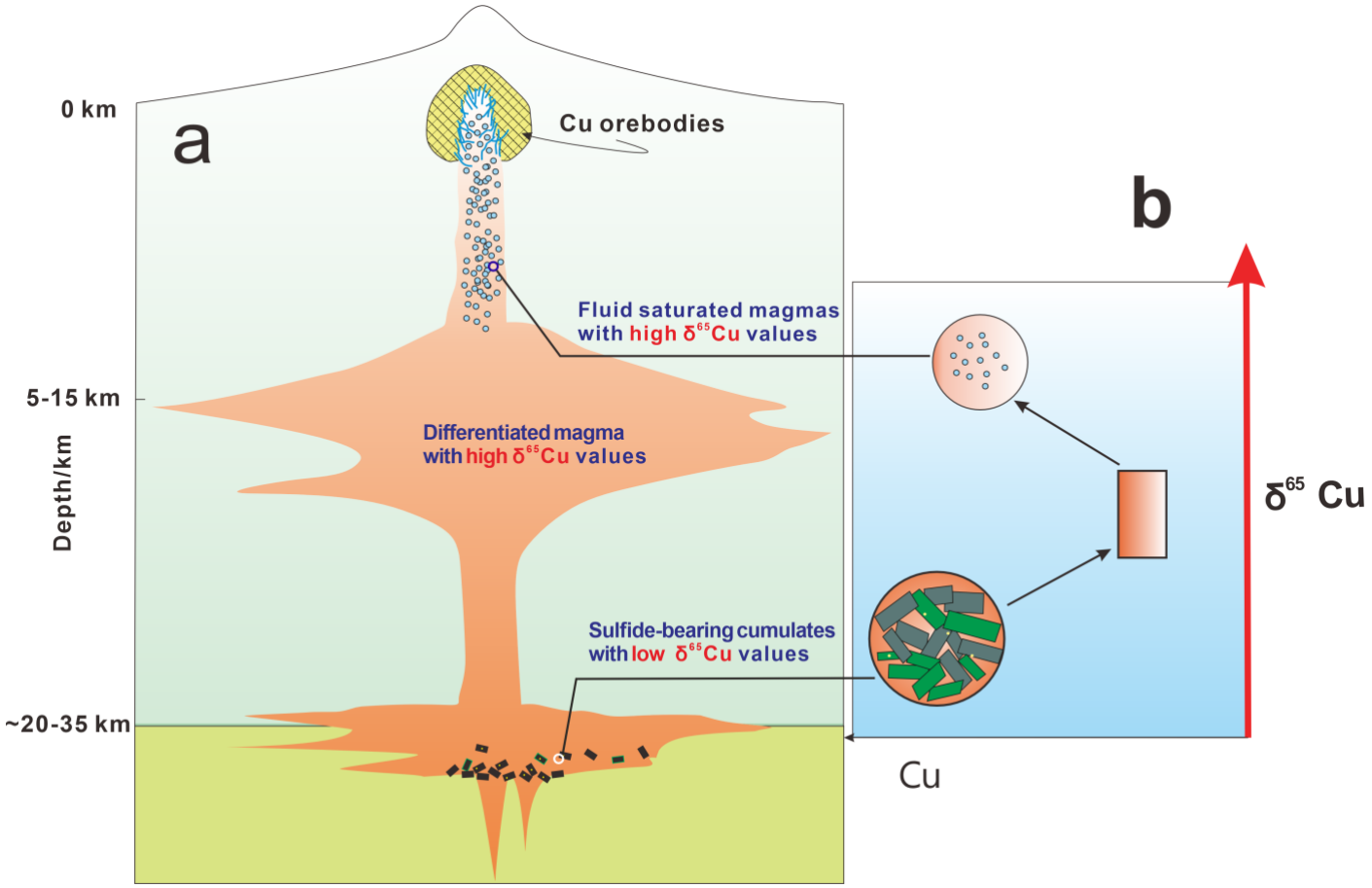

Figure S-5 A schematic model for early sulfide saturation at depth and late-fluid saturation in the porphyry Cu deposits system. **(a)** Sulfide accumulation during amphibole differentiation of mantle-derived magmas results in enrichment of the lighter Cu isotopes in sulfide-rich cumulates and, leaving behind differentiated ore-forming magmas characterized by low Cu content and high δ^{65}Cu; **(b)** when the evolved magmas further experience fluid saturation at magmatic temperatures (800-850 °C), a high δ^{65}Cu will may be imparted.

Supplementary Information References

Chen, C.J., Chen, B., Li, Z., Wang, Z.Q. (2016) Important role of magma mixing in generating the Mesozoic monzodioritic-granodioritic intrusions related to Cu mineralization,Tongling, East China: Evidence from petrological and in situ Sr–Hf isotopic data. *Lithos* 248–251, 80–93. https://doi.org/10.1016/j.lithos.2016.01.009

Davidson, J., Turner, S., Handley, H., Macpherson, C., Dosseto, A. (2007) Amphibole "sponge"in arc crust? *Geology* 35, 787–790. https://doi.org/10.1130/G23637A.1

Du, J.G., Audétat, A. (2020) Early sulfide saturation is not detrimental to porphyry Cu-Au formation. *Geology* 48, 519–524. https://doi.org/10.1130/G47169.1

Du, J.G., Du, Y.S., Cao, Y., Tu, W. (2016) Geochronology and Geochemical Characteristics of the Jiaochong Dioritic Porphyrite Intrusion in Tongling and Its Metallogenitic Significance, Anhui Province. *Bulletin of Mineralogy, Petrology and Geochemistry* 34, 804–811 [in Chinese with English abstract]. https://doi.org/10.3969/j.issn.1007-2802.2015.04.015

Du, J.G., Du, Y.S., Cao, Y. (2018) Important role of hornblende fractionation in generating the adakitic magmas in Tongling, Eastern China: Evidence from amphibole megacryst and cumulate xenoliths and host gabbros. *International Geology Review* 60, 1–23. https://doi.org/10.1080/00206814.2017.1418683

Du, J.G., Deng, X.H., Du, Y.S., Wang, G.W. (2025) Amphibole fractionation controls the redox state of magmas in porphyry Cu ore systems: Constraints from amphibole-rich rocks in eastern China. *GSA Bulletin* 137, 2703–2718. https://doi.org/10.1130/B37687.1

Guo, H., Lu, J., Jiang, S., Zhang, R., Zhao, Z. (2013) Chronology, Hf isotopes, geochemistry, and petrogenesis of the magmatic rocks in the Shizishan ore field of Tongling, Anhui province. *Science China Earth Sciences* 56, 993–1013. https://doi.org/10.1007/s11430-013-4589-2

Huang, S., Xu, Z., Gu, L. (2004) A discussion on geochemical characteristics and genesis of intrusions in Shizishan orefield, Tongling area, Anhui Province. *Geological Journal of China Universities* 10, 217–226. https://geology.nju.edu.cn/EN/Y2004/V10/I2/217

Hu, L., Li, Y., Song, Y., Wang, A. (2018) Zircon U-Pb dating and mineral Chemistry of the amphibole cumulates in Tongling, Anhui Province, and its implications for deep magmatism. *Acta Geologica Sinica* 92, 704–721 [in Chinese with English abstract].

Lai, X.D., Yang, X.Y., Sun, W.D., Cao, X.S. (2012) Chronological-geochemical characteristics of the Shujiadian Intrusion, Tongling Ore Cluster Field: Its significance to metallogenesis. *Acta Geologica Sinica* 86, 470–485 [in Chinese with English abstract].

Li, S., Yang, X.Y., Huang, Y., Sun, W.D. (2014) Petrogenesis and mineralization of the Fenghuangshan skarn Cu-Au deposit, Tongling ore cluster field, Lower Yangtze metallogenic belt. *Ore Geology Reviews* 58, 148–162. https://doi.org/10.1016/j.oregeorev.2013.11.004

Liu, Y., Hu, Z., Gao, S., Günther, D., Xu, J., Gao, C., Chen, H. (2008) In situ analysis of major and trace elements of anhydrous minerals by LA-ICP-MS without applying an internal standard. *Chemical Geology* 257, 34-43 https://doi.org/10.1016/j.chemgeo.2008.08.004

Loucks, R.R. (2014) Distinctive composition of copper-ore-forming arc magmas. *Australian Journal of Earth Sciences* 61, 5–16. https://doi.org/10.1080/08120099.2013.865676

Neave, D., Putirka, K. (2017) A new clinopyroxene-liquid barometer, and implications for magma storage pressures under Icelandic rift zones. *American Mineralogist* 102, 777–794. https://doi.org/10.2138/am-2017-5968

Putirka, K.D. (2008) Thermometers and barometers for volcanic systems. *Reviews in Mineralogy and Geochemistry* 69, 61–120. https://doi.org/10.2138/rmg.2008.69.3

Putirka, K.D. (2016) Amphibole thermometers and barometers for igneous systems and some implications for eruption mechanisms of felsic magmas at arc volcanoes. *American Mineralogist* 101, 841–858. https://doi.org/10.2138/am-2016-5506

Ridolfi, F., Renzulli, A., Puerini, M. (2010) Stability and chemical equilibrium of amphibole in calc-alkaline magmas: An overview, new thermobarometric formulations and application to subduction-related

volcanoes. *Contributions to Mineralogy and Petrology* 160, 45–66. https://doi.org/10.1007/s00410-009-0465-7

Wang, Q., Xu, J., Zhao, Z., Xiong, X., Bao, Z. (2003) Petrogenesis of the Mesozoic intrusive rocks in the Tongling area, Anhui Province, China and their constraint on geodynamic process. *Science in China Series D: Earth Sciences* 46, 801–815. https://doi.org/10.1007/BF02879524

Wang, S., Zhou, T., Yuan, F., Fan, Y., Zhang, L., Song, Y. (2015) Petrogenesis of Dongguashan skarn-porphyry Cu–Au deposit related intrusion in the Tongling district, eastern China: Geochronological, mineralogical, geochemical and Hf isotopic evidence. *Ore Geology Reviews* 64, 53–70. https://doi.org/10.1016/j.oregeorev.2014.06.012

Wang, S., Zhou, T., Yuan, F., Cooke, D.R., Zhang, L., Fu, B., White, N.C. (2016) Geochemical characteristics of the Shujiadian Cu deposit related intrusion in Tongling: Petrogenesis and implications for the formation of porphyry Cu systems in the Middle-Lower Yangtze River Valley metallogenic belt, Eastern China. *Lithos* 252–253, 185–199. https://doi.org/10.1016/j.lithos.2016.02.013

Wu, C., Gao, Q., Guo, H., Guo, X., Liu, L., Gao, Y., Lei, M., Qin, H. (2010) Petrogenesis of the intermediate-acid intrusive rocks and zircon SHRIMP dating in Tongling, Anhui, China. *Acta Petrologica Sinica* 26, 2630–2652 [in Chinese with English abstract].

Xie, J.C., Yang, X.Y., Du, J.G., Sun, W.D. (2008) Zircon U-Pb geochronology of the Mesozoic intrusive rocks in the Tongling region: Implications for copper-gold mineralization. *Acta Petrologica Sinica* 24, 1782–1800 [in Chinese].

Xie, J.C., Yang, X.Y., Sun, W.D., Du, J.G., Xu, W., Wu, L.B., Wang, K.Y., Du, X.W. (2009) Geochronological and geochemical constraints on formation of the Tongling metal deposits, middle Yangtze metallogenic belt, east-central China. *International Geology Review* 51, 388–421. https://doi.org/10.1080/00206810802712004

Xie, J., Chen, S., Sun, W., Yang, X. (2012a) Geochemistry of Early Cretaceous adakitic rocks in Tongling region of Anhui Province: Constraints for rock- and ore-forming. *Acta Petrologica Sinica* 28, 3181–3196 [in Chinese].

Xie, J., Yang, X., Sun, W., Du, J. (2012b) Early Cretaceous dioritic rocks in the Tongling region, eastern China: Implications for the tectonic settings. *Lithos* 150, 49–61. https://doi.org/10.1016/j.lithos.2012.05.008

Yan, J., Chen, J., Xu, X. (2008) Geochemistry of Cretaceous mafic rocks from the Lower Yangtze region, eastern China: Characteristics and evolution of the lithospheric mantle. *Journal of Asian Earth Sciences* 33, 177–193. https://doi.org/10.1016/j.jseaes.2007.11.002

Yang, X.N., Xu, Z.W., Lu, X.C., Jiang, S.Y., Ling, H.F., Liu, L.G., Chen, D.Y. (2011) Porphyry and skarn Au-Cu deposits in the Shizishan orefield, Tongling, East China: U-Pb dating and in situ Hf isotope analysis of zircons and petrogenesis of associated granitoids. *Ore Geology Reviews* 43, 182–193. https://doi.org/10.1016/j.oregeorev.2010.09.003